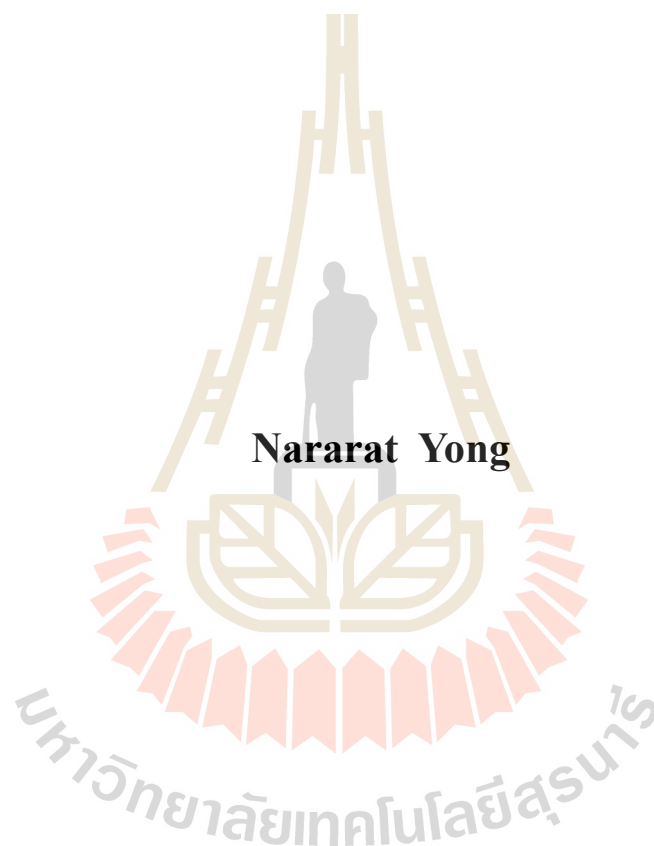# STRUCTURE AND THERMOELECTRIC PROPERTIES

OF ALUMINUM AND MANGANESE DOPED

ZINC OXIDE

Nararat Yong

A Thesis Submitted in Partial Fulfillment of the Requirements for the

Degree of Master of Science in Chemistry

Suranaree University of Technology

Academic Year 2016

โครงสร้างและสมบัติเทอร์โมอิเล็กทริกของสารประกอบซิงค์ออกไซด์
เจืออลูมินัมและแมงกานีส

นางสาวนรารัตน์ ยงค์

วิทยานิพนธ์นี้เป็นส่วนหนึ่งของการศึกษาตามหลักสูตรปริญญาวิทยาศาสตรมหาบัณฑิต
สาขาวิชาเคมี
มหาวิทยาลัยเทคโนโลยีสุรนารี
ปีการศึกษา 2559

STRUCTURE AND THERMOELECTRIC PROPERTIES

OF ALUMINUM AND MANGANESE DOPED

ZINC OXIDE

Suranaree University of Technology has approved this thesis submitted in partial fulfillment of the requirements for a Master's Degree.

Thesis Examining Committee

_____

(Assoc. Prof. Dr. Jatuporn Wittayakun)

Chairperson

_____

(Asst. Prof. Dr. Theeranun Siritanon)

Member (Thesis Advisor)

_____

(Asst. Prof. Dr. Sanchai Prayoonpokarach)

Member

_____

(Asst. Prof. Dr. Rapee Utke)

Member

_____   _____

(Prof. Dr. Sukit Limpijumnong)   (Prof. Dr. Santi Maensiri)

Vice Rector for Academic Affairs   Dean of Institute of Science

and Innovation

นรารัตน์ ยงค์ : โครงสร้างและสมบัติเทอร์โมอิเล็กทริกของสารประกอบซิงค์ออกไซด์เจือ
อลูมินัมและแมงกานีส (STRUCTURE AND THERMOELECTRIC PROPERTIES OF
ALUMINUM AND MANGANESE DOPED ZINC OXIDE). อาจารย์ที่ปรึกษา :
ผู้ช่วยศาสตราจารย์ ดร.ธีรนันท์ ศิริตานนท์, 68 หน้า.

ผลของการแทนที่แบบเดี่ยวและแบบคู่ของอลูมินัม (Al) และแมงกานีส (Mn) ต่อโครงสร้าง
องค์ประกอบทางเคมีและคุณสมบัติเทอร์โมอิเล็กทริกของซิงค์ออกไซด์ (ZnO) ได้ถูกศึกษาใน
สารประกอบสามกลุ่มได้แก่ $Zn_{1-2x}Al_{2x}O$, $Zn_{1-2x}Mn_{2x}O$ and $Zn_{1-2x}Al_xMn_xO$ (x = 0, 0.01, 0.02, 0.03,
0.04) สารตัวอย่างทั้งหมดถูกสังเคราะห์ด้วยวิธีการสลายตัวด้วยความร้อน การแทนที่ซิงค์ด้วย
อลูมินัมและแมงกานีสไม่มีผลต่อโครงสร้างของซิงค์ออกไซด์แต่มีผลต่อสมบัติทางไฟฟ้าของสาร
การแทนที่ซิงค์ด้วยอลูมินัมในปริมาณเล็กน้อยมีผลทำให้ความนำไฟฟ้าของสารเพิ่มขึ้นแต่ทำให้
สัมประสิทธิ์ซีเบคลดลงในขณะที่การแทนที่ด้วยแมงกานีสทำให้สัมประสิทธิ์ซีเบคเพิ่มขึ้นอย่างมาก
แต่ทำให้ความนำไฟฟ้าลดลงสารตัวอย่างที่มีการแทนที่แบบคู่แสดงผลจากทั้งสองไอออน อย่างไรก็
ตาม การเปลี่ยนแปลงในความนำไฟฟ้ามีความโดดเด่นมากและมีอิทธิพลต่อการคำนวณค่า Power
factor มากกว่า ดังนั้นสารตัวอย่างที่มีความนำไฟฟ้ามากที่สุดในงานวิจัยนี้ซึ่งได้แก่ $Zn_{0.98}Al_{0.02}O$
แสดงค่า Power factor สูงที่สุดเท่ากับ 1.03×10^{-4} $WK^{-2}m^{-1}$ ที่อุณหภูมิ 800 เคลวิน ในขณะที่สาร
ตัวอย่างที่มีการแทนที่แบบคู่ที่ให้ค่า Power factor ดีที่สุด ได้แก่ $Zn_{0.98}Al_{0.01}Mn_{0.01}O$ ซึ่งมี Power
factor เท่ากับ 4.79×10^{-5} $WK^{-2}m^{-1}$ ที่อุณหภูมิเดียวกัน

สาขาวิชาเคมี
ปีการศึกษา 2559

ลายมือชื่อนักศึกษา_____
ลายมือชื่ออาจารย์ที่ปรึกษา_____

NARARAT YONG : STRUCTURE AND THERMOELECTRIC PROPERTIES OF ALUMINUM AND MANGANESE DOPED ZINC OXIDE. THESIS ADVISOR : ASST. PROF. THEERANUN SIRITANON, Ph.D. 68 PP.

THERMOELECTRICS/ELECTRICAL PROPERTIES/OXIDES/ THERMAL DECOMPOSITION METHOD

The effect of Al and Mn single and double substitution on structure, chemical composition, and thermoelectric properties of ZnO was investigated in three series of compounds; $Zn_{1-2x}Al_{2x}O$, $Zn_{1-2x}Mn_{2x}O$, and $Zn_{1-2x}Al_xMn_xO$ (x = 0, 0.01, 0.02, 0.03, 0.04). All samples were synthesized by thermal decomposition method. Substituting Al and Mn do not affect ZnO structure but affects its electrical properties. Replacing Zn by a small amount of Al lead to an increase in electronic conductivity but a decrease in absolute Seebeck coefficient. On the other hand, Mn substitution increases absolute value of Seebeck coefficient but decreases the electronic conductivity. Double substituted samples exhibit the effects from both ions. Nevertheless, the change in electronic conductivity is more pronounced and dominant in the power factor calculation. Thus the most conductive sample in this work, $Zn_{0.98}Al_{0.02}O$, shows the highest power factor of 1.03×10^{-4} $WK^{-2}m^{-1}$ at 800 K while the best double substituted sample, $Zn_{0.98}Mn_{0.01}Al_{0.01}O$, gives a power factor of 4.79×10^{-5} $WK^{-2}m^{-1}$ at the same temperature.

School of Chemistry   Student's Signature_____ __

Academic Year 2016   Advisor's Signature_____

ACKNOWLEDGEMENTS

First of all, I would like to express my sincere thanks to my advisor, Asst. Prof. Dr. Theeranun Siritanon for her endless guidance, support, motivation, encouragement, and patient help during my study and throughout the project. Thank you very much for giving me this wonderful opportunity. I think I am very lucky to have a chance to learn from her. Under her guidance and encouragement, I successfully surpassed many difficulties and learned a lot. She gave enough freedom during my research to encourage me to become an independent thinker. I appreciate all knowledge I gained from her. She is an excellent advisor as she is reasonable, positive, and kind. She taught me how to be a diligent, patient, and reasonable person who thinks positively. She gave consolation for me every time when I had problems. I really appreciate everything she has given me. She is a great advisor.

I also would like to acknowledge the committees including Assoc. Prof. Dr. Jatuporn Wittayakun, Asst. Prof. Dr. Sanchai Prayoonpokarach, and Asst. Prof. Dr. Rapee Utke. Their comments and suggestions were very useful for my thesis.

I also would like to express my appreciation to Dr. Pinit Kitkhonthod, Dr. Norong Chanlek, and Dr. Nirawat Thamajak for their valuable discussions and assistance in my experiments. XANES measurement in this work was supported by the SUT-NANOTEC-SLRI Joint Research Facility for XAS beamtime.

I am thankful to Dr. Adul Harnwangmuang for providing his laboratory and Mr. Dangdesh Naenkieng for measurement the thermoelectric properties of the

samples. Thermoelectric properties measurement in this work was supported by the Thermoelectric and Nanotechnology Research Center, Faculty of Science and Technology, Rajamangala University of Technology Suvarnabhumi.

I am thankful to Dr. Sojiphong Chatraphorn and Semiconductor Physics Research Laboratory, Department of Physics, Chulalongkorn University for Hall measurements.

All experiments in this work could not have been done without the help and support from the people of Suranaree University of Technology: the research group member, colleagues in the School of Chemistry, colleagues in the School of Physics, and office staffs in the Center for Scientific and Technological Equipment. Also, many thanks for the Center for Scientific and Technological Equipment (CSTE) for providing facilities for my research.

Importantly, I would like to acknowledge the National Research Council of Thailand and Suranaree University of Technology for financial supports.

Last but not least, words cannot describe my gratitude. I want to express my deepest appreciation to my entire family for their sincere love, endless love, encouragement, support, and inspirations throughout my study.

Nararat Yong

CONTENTS

CONTENTS (Continued)

CONTENTS (Continued)

LIST OF TABLES

LIST OF FIGURES

LIST OF FIGURES (Continued)

LIST OF FIGURES (Continued)

LIST OF ABBREVIATIONS AND SYMBOLS

e	Electric charge
μ	Carrier mobility
σ	Electrical conductivity
ρ	Electrical resistivity
κ_{ph}	Phonon thermal conductivity
κ_{el}	Electronic thermal conductivity
Ω	Ohm
κ	Thermal conductivity
λ	Wavelength
d	Spacing between the planes in an atomic
eV	Electron Volt
A	Transport constant
N_c	Density of state
q	Electrical charge
DMF	Dimethylformamide
EDS	Energy Dispersive X-ray Spectroscopy
SEM	Emission Scanning Electron Microscopy
FT-IR	Fourier Transform Infrared Spectroscopy
XAS	X-ray Absorption Spectroscopy

LIST OF ABBREVIATIONS (Continued)

XANES	X-ray Absorption Near Edge Spectroscopy
XRD	X-ray Diffraction
XRD	X-ray Diffraction
TGA	Thermogravimetric Analysis
I	Electric current
R	Resistance
k_B	Boltzmann constant
L	Lorentz factor
V_H	Hall voltage
B	Magnetic field
d	Sample thickness
S	Seebeck coefficient
T	Temperature
V	Voltage
W	Watt
ZT	Dimensionless figure of merit

CHAPTER I

INTRODUCTION

1.1 Introduction

The thermoelectric energy conversion is a promising technology due to its ability to convert thermal energy directly to electrical energy. Nowadays, more than half of all energy produced is lost as waste heat into the environment without any applications. Thermoelectric energy recycles wasted heat into electricity. Its properties allow applications on both electrical power generation and various electronic cooling devices (Funahashi *et al.*, 2011). The efficiency of thermoelectric materials depends on material properties which can be determined by the dimensionless figure of merit, ZT, where $ZT = \frac{S^2 \sigma T}{\kappa}$, S is the Seebeck coefficient, σ is the electrical conductivity and κ is the thermal conductivity. Good thermoelectric materials should have high ZT thus they should have large Seebeck coefficient, high electrical conductivity, and low thermal conductivity.

Several good thermoelectric materials are alloys such as Bi_2Te_3, PbTe, and $Si_{1-x}Ge_x$ (Mahan, 1998; Sales *et al.*, 1996; Yamashita *et al.*, 2003). However, their uses are limited at low temperatures as they have low stability and high toxicity. In contrast, oxides are more environmental-friendly and have excellent thermal and chemical stability. As they are chemically stable at high temperature in air,

thermoelectric oxides are expected to be used in broader applications (Cheng *et. al*., 2006).

Some oxide materials have been discovered with good thermoelectric properties. They include $CaMnO_3$-based perovskites, ZnO-based oxide, layered cobalt oxides represented by $NaCo_2O_4$ and $Ca_3Co_4O_9$, and $SrTiO_3$-related phases (Ohtaki *et al*., 1997). Oxide materials are obviously very attractive. Among them, ZnO is a promising thermoelectric material showing a fairly high figure of merit, ZT. It is naturally n-type wide-band gap semiconductor (Ohtaki *et al*., 1996) with excellent charge carrier transport properties (Jood *et al*., 2011) at elevated temperatures in air (Koumoto *et al*., 2006).

Doped ZnO has gained lots of attention in thermoelectric field especially in high temperature applications. Effects of several dopants on thermoelectric properties of ZnO have been investigated. It is generally known that Al doping increases electrical conductivity of ZnO (Ohtaki *et al*., 1996; Tsubuta *et al*., 1997). Although there are no reports on thermoelectric properties of Mn-doped ZnO polycrystalline samples, Mn has been reported to increase Seebeck coefficient of ZnO in thin film (Ghosh *et al*., 2007) and it is likely to have the same effects in polycrystalline samples as well.

This study focuses on improving the thermoelectric properties of zinc oxide by doping. The influences of aluminum and/or manganese doping on thermoelectric properties are evaluated. Structural details of the compounds and the relationships between structure, compositions, and properties are investigated. The current research presents a strategy to improve the thermoelectric properties of ZnO by double

substitution of Al and Mn in $Zn_{1-2x}Al_xMn_xO$ where the combined positive effects of both dopants are expected to further improve thermoelectric performance of the materials. Series of compounds including $Zn_{1-x}Al_xO$, $Zn_{1-x}Mn_xO$ (x= 0.02, 0.04, 0.06 and 0.08) and $Zn_{1-2x}Al_xMn_xO$ (x= 0.01, 0.02, 0.03 and 0.04) have been prepared by thermal decomposition method and characterized with several techniques. The obtained results are used to discuss the effects of Al and/or Mn substitution on structure and thermoelectric properties of ZnO.

1.2 References

Cheng, J., Sui, Y., Fu, H., Lu, Z., Wei, B., Qian, Z., Miao, J., Liu, Z., Huang, X., Zhu, R., Wang, X., and Su, W. (2006). Fabrication and thermoelectric properties of highly texture $NaCo_2O_4$ ceramic. **J. Alloy. Compd.** 407: 299-303.

Funahashi, R. (2011). Waste heat recovery using thermoelectric oxide materials. **Sci. Adv. Mater.** 3: 682-686.

Ghosh, C. K., Das, S., and Chattopadhyay, K.K. (2007). Enahancement of thermopower of Mn doped ZnO thin film. **Physica B.** 399: 38-46.

Jood, P., Metha, J.R., Zhang, Y., Peleckis, G., Wang, X., Siegel, X.R., Tascius, B.T., Dou, XS., and Rammanath, G. (2011). Al-doped zinc oxide nanocomposites with enhanced thermoelectric properties. **Nano Lett.** 11: 4337-4342.

Koumoto, K., Terasaki, I., and Funahashi, R., (2006). Complex oxide materials for potential thermoelectric applications.**Mater. Res. Bull.** 31: 206-210.

Mahan, G. D. (1998). Good thermoelectrics. **Solid State Phys.** 51: 81-157.

Ohtaki, M. (1997). Recent aspects of oxide thermoelectric materials for power generation from mid-to-high temperature heat source. **J. Ceram. Soc. Jpn.** 119: 770-775.

Ohtaki, M., Thubota, T., Eguchi, K., and Arai, H. (1996). High temperature thermoelectric properties of $(Zn_{1-x}Al_x)O$. **J. Appl. Phys.** 79: 1816.

Sales, B. C., Mandrus, D., and Williams, R. K. (1996). Filled skutteruditeantimonides: a new class of thermoelectric materials. **Sci.** 272: 1325-1328.

Tsubota, T., Ohtaki, M., Eguchi, K., and Arai, H. (1997). Thermoelectric properties of Al-doped ZnO as a promising oxide material for high-temperture thermoelectric conversion. **J. Mater. Chem.** 7: 85-90.

Yamashita, O., Tomiyoshi, S., and Makita, K. (2003).Bismuth telluride compounds with high thermoelectric figures of merit. **J. Appl. Phys.** 93: 368-374.
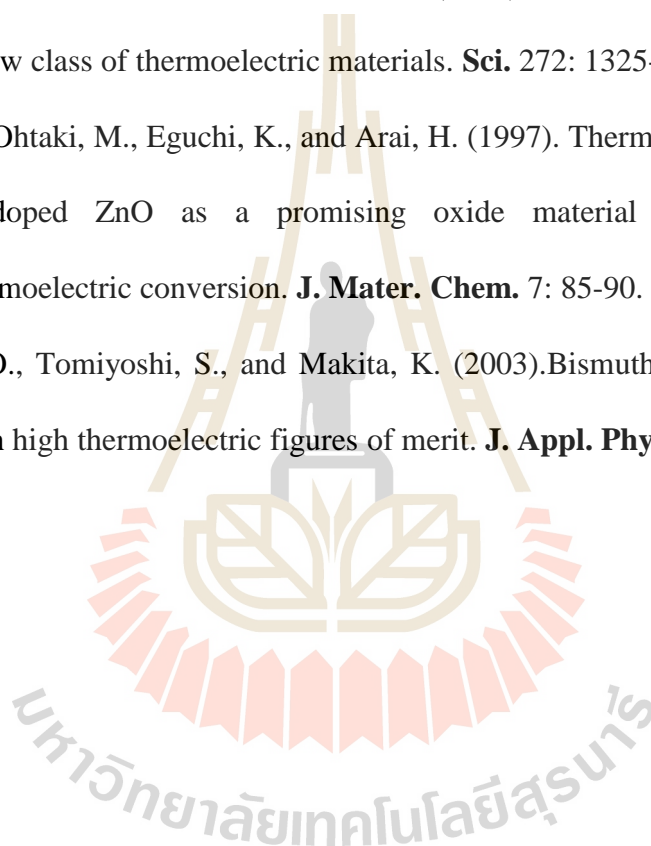
CHAPTER II

LITERATURE REVIEW

2.1 Thermoelectric materials

Thermoelectric materials exhibit the phenomenon of heat and electricity conversion on two important effects, Seebeck (Seebeck, 1823) and Peltier effects (Peltier, 1834). The Seebeck effect is a development of voltage across the junction of two different materials held at different temperatures. It is shown as power generation mode in Figure 2.1. On the other hand, the Peltier effect involves a heat liberation or absorption when electrical current is applied to such junction, which is shown as refrigeration mode in Figure 2.1.

(a) Refrigeration Mode   (b) Power-generation Mode
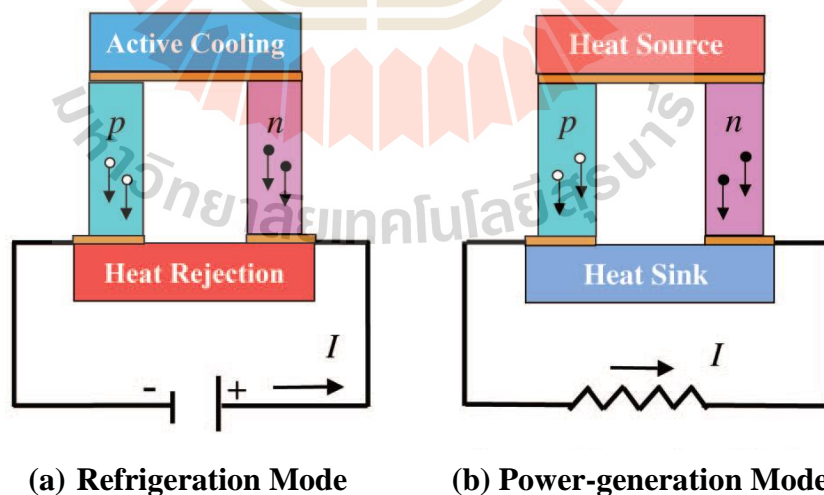
Figure 2.1 Diagram of a thermoelectric device made of n-type and p-type materials in (a) a refrigeration and (b) a power-generation modes (Tritt and Subramanian, 2006).

The performance of a thermoelectric material is defined by the dimensionless figure of merit, ZT;

$$ZT = \frac{S^2\sigma T}{\kappa} = \frac{S^2 T}{\rho\kappa} \tag{1}$$

where S is the Seebeck coefficient, σ is the electrical conductivity, ρ is the electrical resistivity, κ is the thermal conductivity ($\kappa = \kappa_{el} + \kappa_{ph}$; κ_{el} and κ_{ph} are the electronic and the lattice components of κ, respectively), and T is the absolute temperature. To maximize the ZT value, high S, high σ, and low κ are simultaneously required. The best thermoelectric materials currently used in devices have $ZT \geq 1$ (Tritt and Subramanian, 2006), hence $ZT \geq 1$ is generally accepted for practical applications (Snyder and Toberer, 2008). However, it is difficult to simultaneously control the three parameters as they are strongly correlated to each other and to carrier concentration, n, of the materials as shown in Figure 2.2 (Ohtaki et al., 2011). In general, a carrier concentration of materials in the range of semiconductors presents large ZT values.
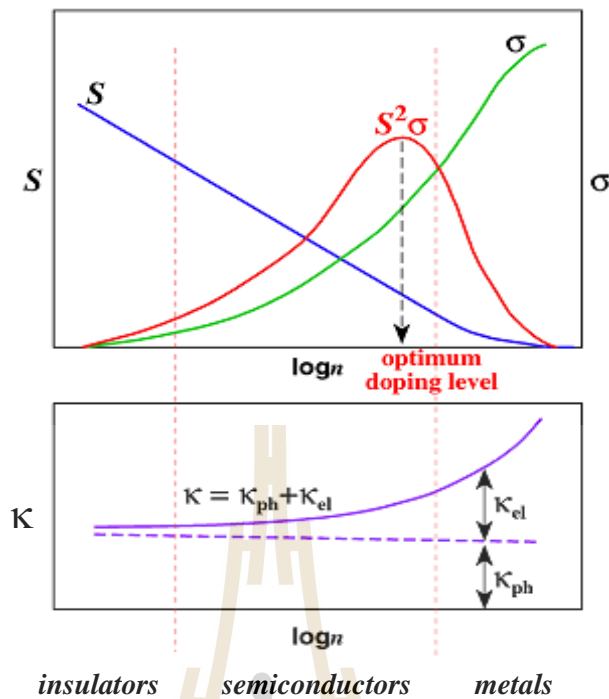
Figure 2.2 Transport properties as a function of carrier concentrations (Ohtaki *et al.*, 2011).

Besides the high ZT value, the operating temperature of a system is also important for real applications. As shown in Figure 2.3, each material has a different range of operating temperature and materials with wider ranges of operating temperatures have more potential for the real applications.

Prices and effects on environment have to be considered when developing appropriate thermoelectric materials. Compounds such as alloys, chalcogenides, and compounds containing heavy elements have limitations when operating at higher temperatures because of their poor durability, low melting point, and high toxicity. Moreover, they are usually expensive. It is therefore necessary to explore new thermoelectric materials to overcome these short comings (Ohtaki *et al.*, 2011).
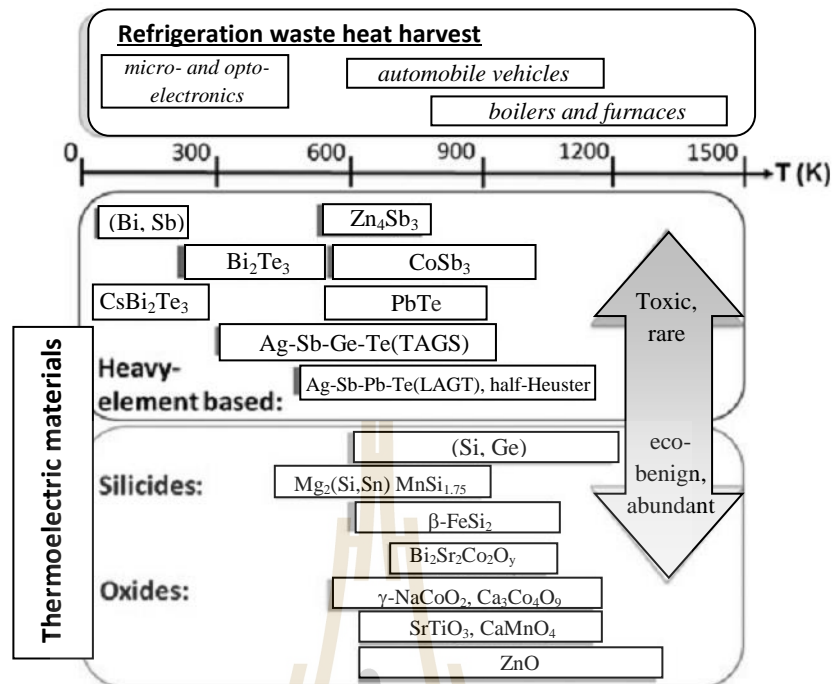
Figure 2.3 Schematic comparisons of various thermoelectric materials for the applications of waste heat harvest and refrigeration in terms of the temperature range of operation, the abundance, and environmental friendliness of constituent elements (He *et al.*, 2011).

2.2 ZnO-based oxides thermoelectric materials

This part discusses the structural details and related researches of the ZnO-related systems.

2.2.1 Structure of zinc oxide

ZnO has the heaxagonal wurtzite structure with space group *P6₃mc*. The structure is characterized by two interconnecting sublattices of Zn^{2+} and O^{2-}, such that each zinc ion is surrounded by a tetrahedral of oxygen ions as shown in Figure 2.4. Zinc oxide is found naturally. It can be doped with donor impurities and changed to an

n-type semiconductor. A zinc atom has a relatively large electronegativity as a metal and these Zn-O bonds are less polarized when compared to other metal-oxygen bonds in metal oxides. Moreover, although the ratio of the ionic radii of Zn^{2+} and O^{2-} geometrically require a 6-fold coordination of O^{2-} around Zn^{2+}, Zn^{2+} prefers 4-fold and the wurtzite structure has much less packing efficiency than that of the closest-packing. Both the less polarized Zn-O bond and the 4-fold coordination suggest the large covalency in ZnO.
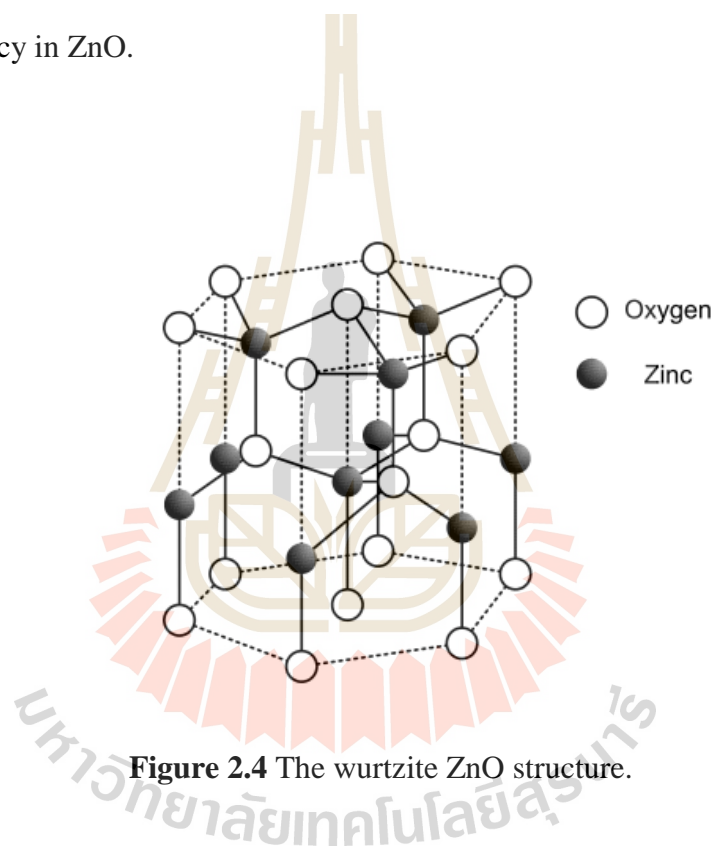
Figure 2.4 The wurtzite ZnO structure.

2.2.2 Thermoelectric properties of ZnO-based oxides

ZnO is an n-type semiconducting material with a direct band gap of 3.37 eV at room temperature (Janotti *et al*., 2009). It has been widely studied since 1935 (Bunn *et al*., 1935). Zn-related materials are attractive in thermoelectric field due to its high Seebeck coefficient at high temperature (Kim *et al*., 2005) as shown in Figure 2.5. However, its practical uses are limited because ZnO has high resistivity and thermal conductivity. ZnO suffers from the high thermal conductivity, 49 $Wm^{-1}K^{-1}$ at 300 K and 10 $Wm^{-1}K^{-1}$ at 1000 K (Tsubota *et al*., 1997), which is very unfavorable for thermoelectric applications. However, ZnO has high carrier mobility of ~200 $cm^2V^{-1}S^{-1}$ at room temperature for n-type doping and 5-50 $cm^2V^{-1}S^{-1}$ at room temperature for p-type doping (Lin *et al*., 2009; Pearton *et al*., 2005) which is suitable for thermoelectric applications.
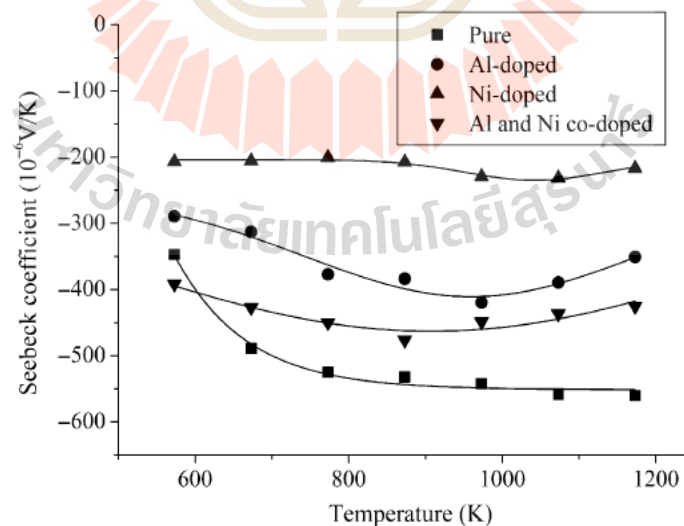
Figure 2.5 Temperature dependence of the Seebeck coefficient of ZnO-based thermoelectric materials (Kim *et al*., 2005).

Numerous strategies have been attempted to generate ZnO related materials with high figure of merit including increasing thermoelectric power and electrical conductivity as well as decreasing thermal conductivity. In this work, double substitution of Al and Mn is investigated as the strategy to improve thermoelectric properties of ZnO.

2.2.2.1 Electrical conductivity improvement

Electrical conductivity (σ) and electrical resistivity (ρ) of materials relates to charge carrier concentration (n), electronic charge (e), and electron mobility (μ) (Snyder and Toberer, 2008)

$$\sigma = \frac{1}{\rho} = ne\mu \qquad (2)$$

Electrical conductivity of the materials can be improved by increasing carrier density and carrier mobility, so one way to improve electrical conductivity is to substitute the materials with heterovalent cations which results in p-type or n-type semiconductors whose major charge carriers are holes and electrons, respectively.

A p-type material can be produced by substituting the parent cations by cations with lower valency which results in generation of positive hole carriers. In ZnO system, it is very difficult to make p-type ZnO, because undoped ZnO with a wurtzite structure occurs naturally as an n-type. However, p-type doping in ZnO may be possible by substitute with group I elements such as Li, Na, and K. (Özgür ü *et al*., 2005).

An n-type material can be produced by substituting the parent cations with higher valency where excess electrons are created as the carriers. Various cations have been used to substitute Zn^{2+} such as group III elements like Al, Ga, Sb, Co etc.

Several elements have been used to make n-type ZnO such as Ga-(Ohtaki *et al*., 2009) In-(Tsubota *et al*., 1997) Mn-(Han *et al*., 2001) Sb-(Park *et al*., 2008) Fe, Ni, and Sm-(Yamakuchi *et al*., 2011). Among all, aluminum is the most common n-type doping (Ohtaki *et al*., 1995; Tsubota *et al*., 1997; Cai *et al*., 2003; Qu *et al*., 2011; Jood *et al*., 2011; Yamakuchi *et al*., 2011; Schäuble *et al*., 2012). Al^{3+} can increase electrical conductivity of ZnO because doping ZnO with Al^{3+} introduces excess electrons. The carrier concentration can be increased from 5.2×10^{17} cm^{-3} in pure ZnO to 7.2×10^{19} cm^{-3} in 2% Al-doped ZnO (Figure 2.6). Despite the high thermal conductivity of ~7 $Wm^{-1}K^{-1}$ at 1273 K, 2% Al-doped ZnO achieved a ZT of ~0.3 at 1273 K owning to high power factor of 1.4×10^{-3} $Wm^{1}K^{-2}$ at the mentioned temperature (Tsubota *et al*., 1997). After that, improvements of electrical conductivity of ZnO have been continually studied and ZT of 0.65 at 1273 K was later obtained by Al, Ga-dually doped ZnO from Ohtaki's work (Ohtaki *et al*., 2009). It was found that co-doping with Al and Ga results in reduction of the thermal conductivity to the value of ~5 $Wm^{-1}K^{-1}$ at 1273 K, while the decrease in the electrical conductivity is relatively small. Moreover, a wider range of operating temperature from 973 to 1673 K and Al content from 0.01 to 0.1 were also investigated (Ohtaki *et al*., 1995).
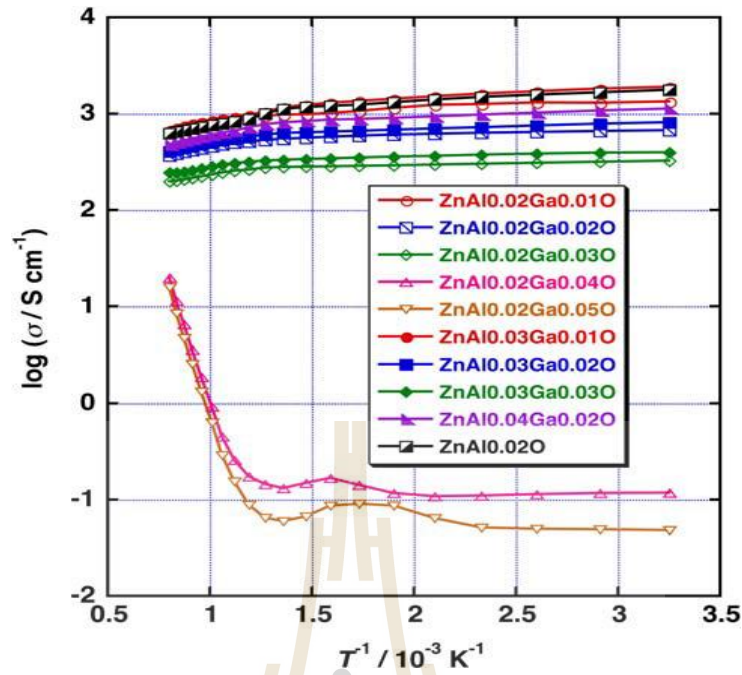
Figure 2.6 The temperature dependence of the electrical conductivity of $Zn_{1-x-y}Al_xGa_yO$ and $(Zn_{0.98}Al_{0.02}O)$ (Ohtaki *et al.*, 2009).

2.2.2.2 Seebeck coefficient improvement

A simplified broad-band model for Seebeck coefficient of extrinsic n-type ZnO semiconductor with negligible hole conduction can be expressed as

$$S = -\frac{k_B}{q}(\ln(\frac{Nc}{n})+A), \qquad (3)$$

where k_B is Boltzmann constant, q is the electronic charge, N_c refers to the density of states, n is the carrier concentration, and A is transport constant (Jantrasee *et al.*, 2014). Therefore, the absolute value of Seebeck coefficient generally decrease when the carrier concentration increases.

Although substitution with cations, e.g. Al-(Ohtaki *et al.*, 1995; Qu *et al.*, 2011), Ga-(Ohtaki *et al.*, 1995), In-(Tsubota *et al.*, 1997) Sb-(Park, K. *et al.*, 2008), Mn-(Han *et al.*, 2001) and Ni, Fe, sm-(Yamaguchi *et al.*, 2011) often increase electrical conductivity, Seebeck coefficients is usually simultaneously decreased. The Seebeck coefficients of Al^{3+}, Ga^{3+}, and In^{3+} substituted ZnO are shown in Figure 2.7. Heterovalent Al- and Ga-doping show relatively constant Seebeck coefficient values. Others result in some variations and the undoped ZnO has higher absolute value of Seebeck coefficient than In and Ga respectively (Tsubota *et al.*, 1997). Al, Ga co-doped ZnO showed higher Seebeck coefficient than Al-doped or Ga-doped ZnO (Figure 2.8). The correlation between electrical conductivity and the Seebeck coefficient is clearly seen in Figure 2.7 as the more resistive undoped ZnO has larger Seebeck coefficient (about -300 to -400 μVK^{-1}) than the conducting ones whose Seebeck coefficients are only about -100 to -200 μVK^{-1}.
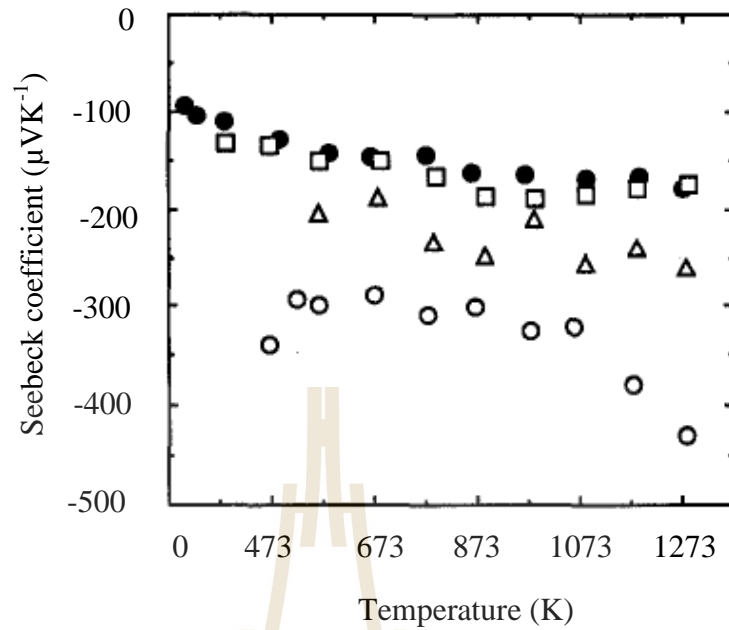
Figure 2.7 The Seebeck coefficient M-doped ZnO and pure ZnO as a function of temperature (M: Zn,○; Al,●;Ga,□; In, Δ, $Zn_{0.98}M_{0.02}O$) (Tsubota *et al*., 1997).
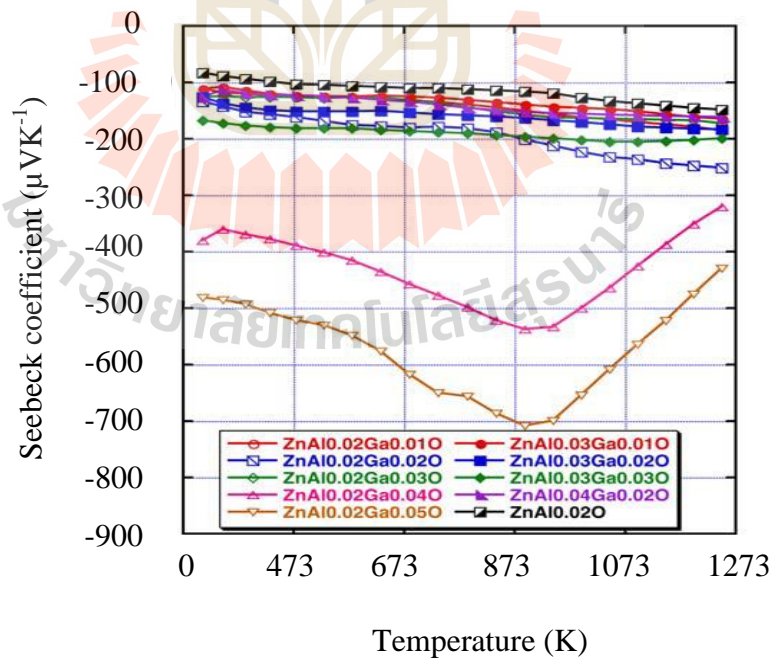
Figure 2.8 Temperature dependence of the Seebeck coefficient of $Zn_{1-x-y}Al_xGa_yO$ ($0.02 \leq x \leq 0.04$, $0 \leq y \leq 0.05$) comparable with $(Zn_{0.98}Al_{0.02})O$ (Ohtaki *et al*., 2009).

In addition, it should be noted that the negative value of Seebeck coefficient of all samples indicates the n-type behavior thus the major carriers are electrons.

Another interesting dopant which shows a rare ability of improving Seebeck coefficient is manganese, Mn^{2+}. Experimental and theoretical works have shown that the unbalancing of up spin and down spin electrons in the conduction band due to the unfilled electrons in Mn d orbital and the hopping contribution caused by unfilled Mn d orbital causes the increase in the Seebeck coefficient of Mn doped ZnO thin film almost linearly as shown in Figure 2.9 (Ghosh *et al*., 2007). Hopping component is due to hopping of electrons between localized states that arises from Mn 3d levels in the band gap. However, there are no reports on Seebeck coefficients of Mn^{2+}-doped ZnO in polycrystalline samples.
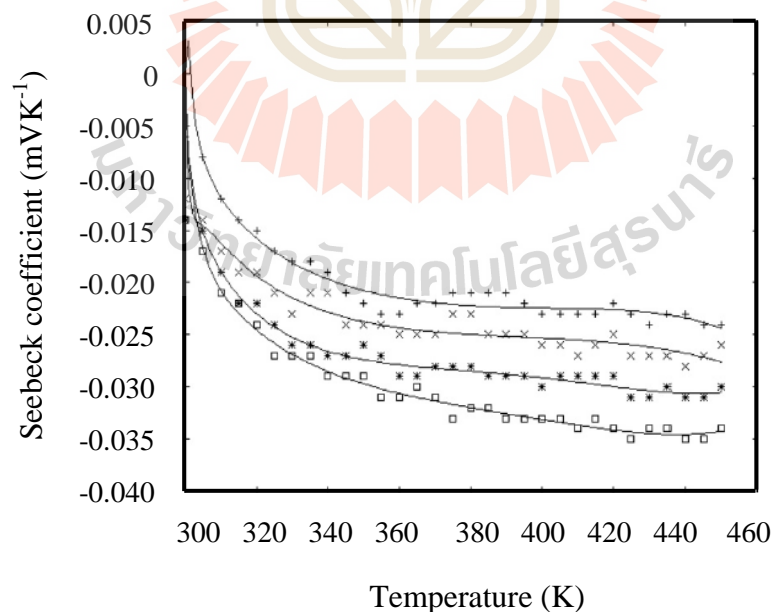
Figure 2.9 Thermoelectric power for different Mn concentration doped ZnO thin film as a function temperature (Ghosh *et al*., 2007).

2.2.2.3 Thermal conductivity improvement

Besides improving electrical conductivity and Seebeck coefficient, the ZT can be further increased by minimizing thermal conductivity. This could be achieved by means of adjusting the crystallographic structure and increasing the phonon scattering. Total thermal conductivity (κ_T) comes from two sources: electronic (κ_{el}) and lattice (κ_{ph}) part. κ_{el} is directly related to the electrical conductivity through the Wiedemann–Franz law:

$$\kappa_{el} = \sigma LT = ne\mu LT \tag{4}$$

where L is the Lorentz factor which is equal to 2.4×10^{-8} $J^2 K^{-2}$ C^{-2} for free electrons. From the relationship, κ_{el} is directly proportional to σ and T.

The average thermal conductivity of ZnO is between 100 and 200 $Wm^{-1}K^{-1}$ (Florescu *et al.*, 2002). There have been several investigations into the enhancing short wave phonon scattering by point defects. For example, co-doped Ga and Al (Ohtaki *et al.*, 2009) showed significant reduction in the value of thermal conductivity to only 5 $Wm^{-1}K^{-1}$ at room temperature (Ohtaki *et al.*, 2009) as shown in Figure 2.10. Zhao *et al.* (2012) also reported that Al substitution decreases the thermal conductivity of ZnO to about 40 $Wm^{-1}K^{-1}$ at room temperature.
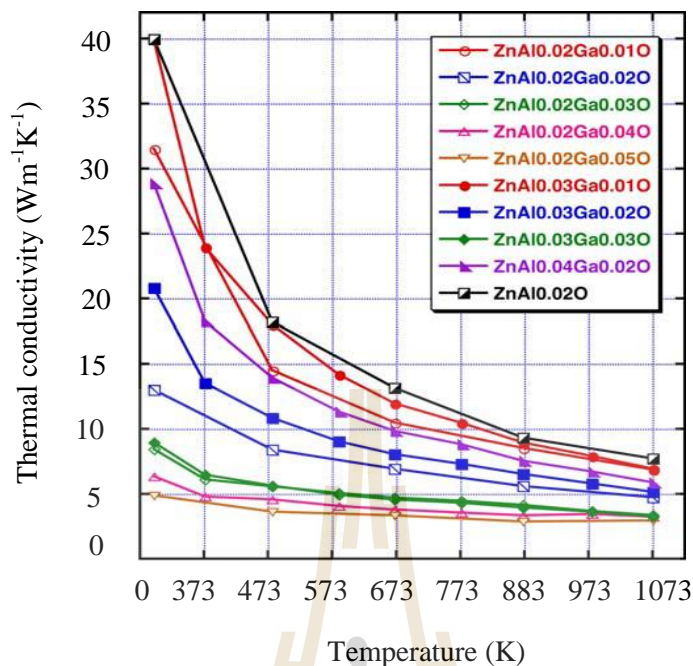
Figure 2.10 Temperature dependence of the thermal conductivity of $Zn_{1-x-y}Al_xGa_yO$ ($0.02 \le x \le 0.04$, $0 \le y \le 0.05$) comparable with $(Zn_{0.98}Al_{0.02})O$ (Ohtaki *et al*., 2009).

2.2.2.4 ZT improvement strategy

ZnO-based oxides have been studied extensively with the main goal of maximizing dimensionless figure of merit, ZT, by substitutions. However, most works have mainly focused on single substitution for the Zn site which leads to improvement of only one or two parameters. There are only a few reports focusing on thermoelectric properties of double-substituted ZnO, the strategy seems valid as it also results in an improved ZT. As each substitution has different effects, the double substitutions are the promising idea to maximize the positive effects on as many parameters as possible and consequently maximize the overall thermoelectric performance.

A good start was obtained by double substitution of Zn site with Al and Ga in $Zn_{1-x-y}Al_xGa_yO$ ($0.02 \leq x \leq 0.04$, $0 \leq y \leq 0.05$) (Ohtaki *et al*., 2009). Al plays an important role in enhancing the conductivity while Ga can both increase Seebeck coefficient and reduce thermal conductivity. As a result, a large ZT was obtained at 1273 K (Ohtaki *et al*., 2009) as shown in Figure 2.11.

The preparation technique also plays an important role in materials properties as it is the main factor to determine particle and grain size, morphology, density, and homogeneity of materials. Sol-gel method, for example, is known to give samples with small particle size which is preferred in thermoelectric materials as it is another way to increase phonon scattering. Moreover, nanocomposites have also been reported to reduce thermal conductivity and consequently improve the ZT as well (Jood *et al*., 2013).

As the concept of double substitution and sample preparation method have been proven to be very useful in achieving high thermoelectric efficiency of ZnO-based materials, they will be the main strategies in this thesis.
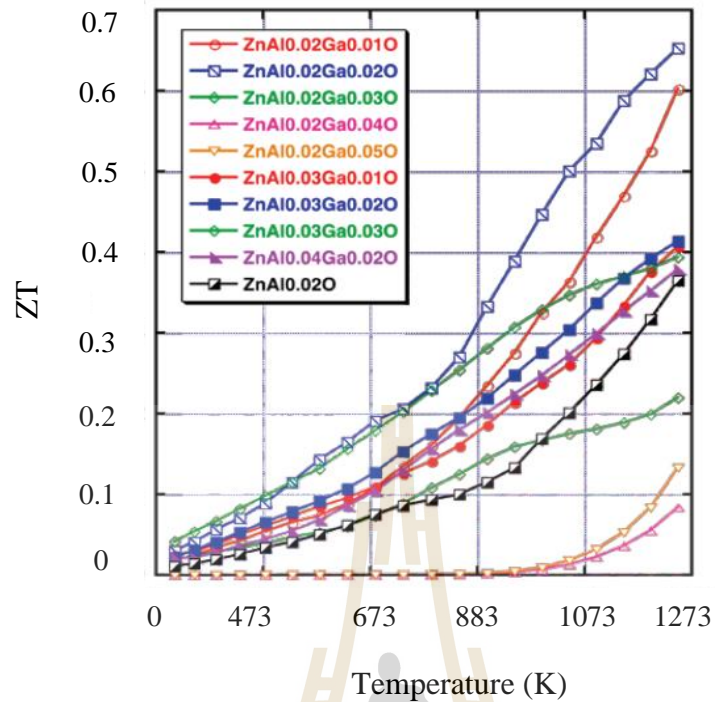
Figure 2.11 Dimensionless figure of merit; ZT, of $Zn_{1-x-y}Al_xGa_yO$ ($0.02 \leq x \leq 0.04$, $0 \leq y \leq 0.05$) comparable with $(Zn_{0.98}Al_{0.02})O$ (Ohtaki *et al.*, 2009).

2.3 Research objectives

1. To prepared Al and Mn single and double substituted ZnO by thermal decomposition method.

2. To study the structure, composition, and thermoelectric properties of the obtained compounds.

3. To explain the effects of synthetic conditions and composition on properties of the obtained compounds.

2.4 References

Bunn, C.W. (1935). A comparative review of ZnO materials and devices. **Proc. Phys. Soc.** 47: 835.

Cai, F.K., Müller, E., Drašar, C., and Mrotzek, A. (2003). Preparation and thermoelectric properties of Al-doped ZnO ceramics. **Mater. Sci. Eng.** 45-48.

Florescu, D.I., Mourokh, L.G., and Polkak, F.H. (2002). High spatial resolution thermal conductivity of bulk ZnO (0001). **J. Appl. Phys.** 91,890.

Ghosh, C.K., Das, S., and Chattopadhyay, K.K. (2007). Enahancement of thermopower of Mn doped ZnO thin film. **Physica B.** 399: 38-46.

Han, J., Matas, P.Q., and Senos, A.M.R. (2001). Efect of Al amd Mn doping on the thermoelectric conductivity of ZnO. **J. Eur. Ceram. Soc.** 21: 183-1886.

He, J., Liu.Y., and Funahashi, R. (2011). Oxide thermoelectrics: the challenges, progress, and outlook. **J. Mater. Res.** 26: 1762-1772.

Jantrasee, S., Pinitsoontorn, S., Moontragoon, P. (2014). First-principles study of the electric structure and thermoelectric properties of Al-doped ZnO. **J. Electron. Mater.** 43: 1689-1695.

Jood, P., Metha, J.R., Zhang, Y., Peleckis, G., Wang, X., Siegel, X.R., Tascius, B.T., Dou, X.S., and Rammanath, G. (2011). Al-doped zinc oxide nanocomposites with enhanced thermoelectric properties. **Nano Lett.** 11: 4337-4342.

Kim, H.K., Shim, H.S., and Shim, B.K. (2005) Microstructural and thermoelectric charecteristics of zinc oxide-based thermoelectric material fabricated using a spark plasma sintering process. **J. Am. Ceram. Soc.** 88: 628-632.

Ohtaki, M. (2011). Recent aspects of oxide thermoelectric materials for power generation from mid-to-high temperature heat source. **J. Ceram. Soc. Jpn.** 119: 770-775.

Ohtaki, M., Arai, K., and Yamamoto, K. (2009). High thermoelectric performance of dually doped ZnO ceramics. **J. Elecron. Mater.** 38:1234-1238.

Ohtaki, M., Thubota, T., Eguchi, K., and Arai, H. (1996). High temperature thermoelectric properties of $(Zn_{1x}Al_x)O$. **J. Appl. Phys.** 79: 1816.

Özgür, Ü., and Morkoc, H. (2009). General properties of ZnO. Published online.

Park, K., Seong, J. K., and Nahm, S. (2008). Improvement of thermoelectric properties with the addition of Sb to ZnO. **J. Alloy. Compd.** 455: 331-335.

Pearton, S.J., Buyanora, I.A., Norton, D.P., Chem, W.M., Zavada, I.M., Hebard, A.F., and Mil, M.P. (2006). ZnO doped, W.M. (2006). ZnO with transition metal ions. IEE Transitioms on Electric Devices. 54: 1040- 1048

Peltier, J.C. (1834). Novelles experiences sur la caloriecete des couranselectriques. **Ann. Chem.** 371-387.

Qu, X., Wang, W., Lv, S., and Jia, D. (2011). Thermoelectric properties and electric structure of Al-doped ZnO. **Solid State Commun.** 151: 332-336.

Schäuble, V.N., Dujardin, R., Weidenkaff, A., and Agurre, H.M. (2012). Influence of thermal aging phenomena on the thermoelectric properties of Al-substituted ZnO. **J. Electron. Mater.** 41: 1607-1614.

Seebeck, T.J. (1823). Magnetischepolarisation der metalle und erzedurcktemperatur-differenz. **Abh. K. Akad. Wiss.** 265-373.

Snyder G.J. and Toberer E.S. (2008).Complex thermoelectric materials. **Nat. Mater.** 7: 105-114.

Tritt, T.M. and Subramanian, M.A. (2006). Thermoelectric materials, phenomena, and applications: a bird's eye view. **Mater. Res. Bull.** 31: 188-198.

Tsubota, T., Ohtaki, M., Eguchi, K., and Arai, H. (1997). Thermoelectric properties of Al-doped ZnO as a promising oxide material for high-temperature thermoelectric conversion. **J. Mater. Chem.** 7: 85-90.

Yamaguchi, H., Chohan, Y., Oda, M., Komiyama, T., Aoyama, T., and Sugiyama, S. (2011). Thermoelectric properties of ZnO ceramics co-doped with Al and transition metals. **J. Electron. Mater.** 40: 723-727.
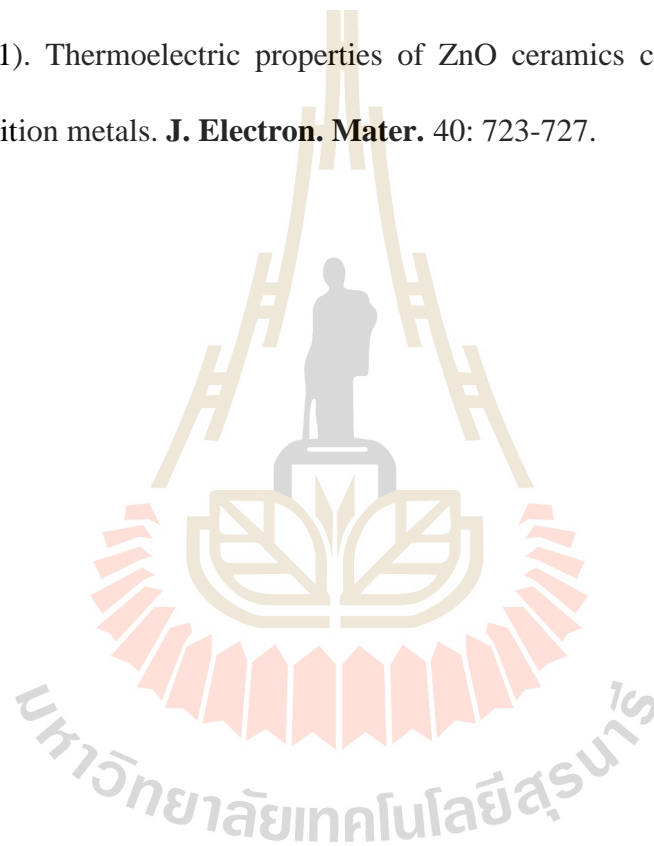
CHAPTER III

EXPERIMENTAL

3.1 Chemicals

- Zinc acetate dihydrate ($Zn(CH_3COO)_2 \cdot 2H_2O$), purity 99.5%, Carlo Erba

- Manganese acetate tetrahydrate ($Mn(CH_3COO)_2 \cdot 4H_2O$), purity 99+%, Acros Organic

- Aluminum nitrate nonahydrate ($Al(NO_3)_3 \cdot 9H_2O$), purity 98-102%, Panreac

- *N*,*N*-dimethylformaminde (DMF), $(CH_3)_2NCH$, purity 99.99%, Carlo Erba

3.2 Instruments

- Stimultaneous Thermal Analyzer (TGA-DSC), Model TGA/DSC1, Metter Toledo

- Fourier transform infrared spectrometer (FT-IR), Tensor 27 Hyperion, Bruker

- Powder X-ray diffractometer (XRD), Model D2 Phaser, Bruker

- Scanning electron microscope (SEM), Model SU5000, HITACHI/Energy dispersive X-ray spectroscopy (EDS), Model Horiba 50 mm^2

- X-ray absorption Spectroscopy (XAS), at SUT-NANOTEC-SLRI XAS beam line (BL5.2) at Synchrotron Light Research Institute (Public organization)

- Simultaneous measurement of Seebeck coefficient and electrical resistivity of thermoelectric materials, Model ZEM-3, ULVAC-RIKO, Inc.

3.3 Sample preparation

3.3.1 Thermal decomposition route

In the thermal decomposition route, a product is obtained by decomposing a solution of mixed metal cations at the designated temperature in desired atmosphere. Thus, it is different from a well known sol-gel technique where a formation of sol and gel is required. Nevertheless, thermal decomposition technique usually allows the synthesis to complete at relatively low temperature because the starting metal cations are mixed in the atomic scale (Siritanon *et al*., 2014).

In this work, the samples of Al, Mn and co-substituted ZnO with nominal compositions $Zn_{1-x}Al_xO$, $Zn_{1-x}Mn_xO$ (x = 0, 0.02, 0.04, 0.06, 0.08), and $Zn_{1-2x}Al_xMn_xO$ (x = 0, 0.01, 0.02, 0.03, 0.04) were synthesized by thermal decomposition route using high purity of zinc acetate $(Zn(CH_3COO)_2 \cdot 2H_2O)$, manganese acetate $(Mn(CH_3COO)_2 \cdot 4H_2O)$ and aluminum nitrate $(Al(NO_3)_2 \cdot 9H_2O)$. Stoichiometric mixtures of zinc acetate, manganese acetate, and aluminum nitrate were dissolved in 30 mL of dimethylformamide. The solutions were stirred with a magnetic stirrer at room temperature. After that, the solutions were dried at 343 K for 4 hours using a hot plate. These samples were later heated at 373 K overnight in the oven for dehydration. The obtained dried solution was ground in an agate mortar by pestle for 15 minutes, placed in Al_2O_3 crucible, and calcined at 623 K for 4 hours at a heating rate of 278 Kmin^{-1}. The calcined powder was ground, pressed into a pellet at 10 MPa, and then sintered at 1673 K for 5 hours in air. A bar-shaped sintered pellet with general dimensions of about 10×3×3 mm was used for the thermoelectric properties measurement.

3.4 Characterizations

3.4.1 Structure identifications

3.4.1.1 Thermogravimetric analysis (TGA)

Thermogravimetric analysis technique analyzes changes in weight of a sample as a function of temperature or time in a controlled atmosphere. Each change in weight refers to the changes of the sample components at each temperature. In this study, thermogravimatric analysis was used to investigate the decomposition of substances and to find the temperature required to decompose all organic species in the samples which determined the calcining temperature.

Thermal decomposition of the dried sample was investigated by TGA using simultaneous thermal analyzer. The dried sample was put in an Al_2O_3 crucible and heated from 298 to 1273 K with a heating rate of 283 $Kmin^{-1}$ in air.

3.4.1.2 Fourier transforms infrared spectroscopy (FT-IR)

This spectroscopic technique is related to the interaction between the compounds and the infrared radiation. The absorption of infrared at specific frequencies is related to vibrations between bonds. An infrared spectrum represents a fingerprint of a sample and can be shown in either the absorption or transmission mode.

In this study, FT-IR was used to probe the structural information of the samples. The presence of specific peaks in the infrared spectra was used to confirm the functional groups of the obtained products.

In the experiment, FT-IR spectra were obtained by Fourier transform infrared spectrometer. The sample was mixed with dry KBr and pressed to form a pellet for the measurement. Spectra were collected in the range 400-4000 cm^{-1} using 64 scans with a resolution of 4 cm^{-1}.

3.4.1.3 X-ray diffraction (XRD)

X-ray diffraction is a principal technique in solid state chemistry which is widely used for crystal structure determination and phase identification. In principle, a monochromatic beam of X-rays strikes the powder of a solid and interacts with electrons. X-ray is scattered in various directions by the electron cloud of the atoms. According to Bragg's equation ($n\lambda = 2d\sin\theta$), the constructive interferences occur with scattered X-rays which are in phase and contribute to X-ray powder diffraction patterns. Each solid material has its own characteristic X-ray powder diffraction pattern.

In this study, the X-ray powder diffraction patterns were used as a fingerprint of samples for phase identification and phase purity confirmation. When a pure phase of a compound is obtained, crystallographic information such as cell parameters would be calculated from the obtained patterns.

In this work, XRD patterns of all samples were collected at room temperature. To check a phase purity, Cu Kα radiation ($\lambda = 0.15406$ Å) with 30 mV and 10 mA was used. The data was collected from diffraction angle (2θ) range of 20° to 80° at the rate of 0.5°/s and the increment of 0.02°. The phase identification and the crystal structure were determined using PDF 36-1451 database and EVA software. To analyze unit cell parameters of the samples, the Le Bail structure refinement method

was performed with TOPAS software using the high quality XRD patterns collected with the diffraction angle (2θ) from 20° to 80° using the increment of 0.01 at the scan speed of 1°/s.

3.4.1.4 Scanning Electron Microscopy (SEM) / Energy Dispersive Spectroscopy (EDS)

This electron microscopy provides the microstructure information on the surface of a sample. SEM is a microscopic technique which produces images of a sample by scanning over it with a focused beam of electrons. The signals resulted from interactions of the electron beam with atoms at or near the surface of the sample produce very high-resolution three-dimension images of sample surface.

During the electron bombardment, X-ray is also produced by the samples. This characteristic X-ray emission relates to the type of the constituent elements and is detected in EDS technique. Thus, a quantitative analysis of an element can be investigated (Smart and Moore, 2005; West, 2014).

In this work, SEM and EDS were used to determine the sample microstructure and its elemental composition. The sintered pellets were coated with gold to make them electrically conduct. All SEM images were taken with a magnification of 5000 to 10000 and the accelerating voltage of 10 kV.

3.4.1.5 X-ray Absorption Near Edge Spectroscopy (XANES)

X-ray Absorption Spectroscopy is an element-specific technique, which measures X-ray absorption of the samples. X-ray absorption near edge structure (XANES) is one type of XAS technique. XANES analysis gives information about the

local structure including oxidation state of elements, and symmetry around the absorbing atoms.

In this work, XANES is used to investigate the valence state of Mn in the samples. Mn-K edge XANES were carried out on polycrystalline samples. MnO, Mn_2O_3, and MnO_2 were used as standard in the measurements. All measurements were conducted at the SUT-NANOTEC-SLRI XAS Beamline (BL5.2), Synchrotron Light Research Insitute (SLRI), Nakhon Ratchasima, Thailand.

3.4.2 Thermoelectric properties characterizations

3.4.2.1 Seebeck coefficient

Seebeck coefficients (S) measure the voltage difference when temperature gradient is applied between two sides of the samples. The absolute values of Seebeck coefficients, in general, increase with the resistivity of the sample. All Seebeck coefficients in this work were measured on the sintered pellets using static method. The electrical current was applied to the hot side of the samples through the metal block to introduce temperature gradient between two sides of the pellet. The voltage across the two sides were measured and the Seebeck coefficient were calculated using $S = \Delta V/\Delta T$ when ΔV and ΔT are voltage difference and temperature difference, respectively (Tritt and Subramanian, 2006).

Seebeck coefficient and electrical resistivity as a function of temperature variation can be measured simultaneously using the ULVAC-RIKO ZEM-3 thermoanalyzer as shown in Figure 3.1. The measurements are performed under inert atmosphere. The instrument consists of a measuring chamber and a controller. Inside a measuring chamber, a bar of sample is set in vertical position

between the upper and lower blocks of electrodes. Voltages across the sample as well as temperature are measured by two probes touching the side of the bar as shown in Figure 3.1b. Seebeck coefficient is obtained using the following relations:

$$\text{Seebeck coefficient} = -(\Delta V/\Delta T) \qquad (5)$$

where ΔV is the voltage difference and ΔT is temperature difference.
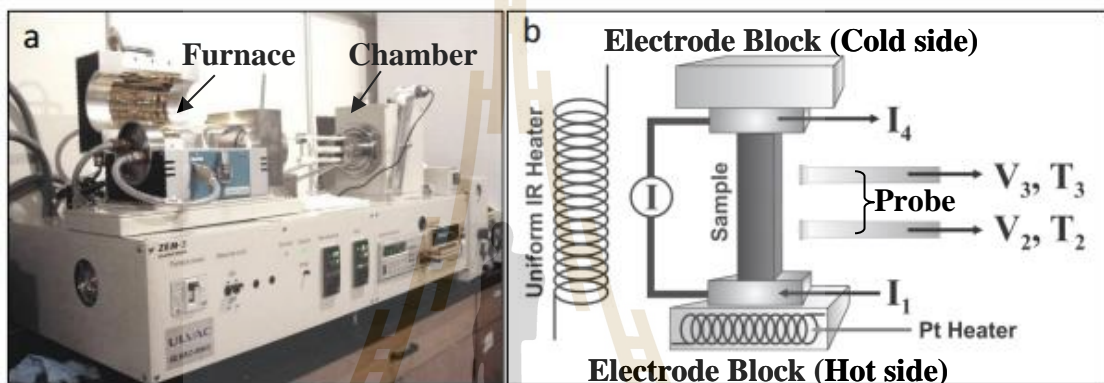
Figure 3.1 The ULVAC-RIKO ZEM-3 instruments (a) and sample in the measuring chamber (b).

3.4.2.2 Electrical resistivity

Electrical resistivity of all samples were measured by the four-probe method. The electrical current was applied to both ends of the bar and the voltage drop was then measured by the two probes touching on its side. Resistance was obtained using the relation: $V = IR$ when I is electrical current, V is voltage, and R is resistance. The obtained resistance was used to calculated the resistivity where resistivity = (resistance $\times$ A)/L; A = surface area and L is the distance between two electrodes as shown in Figure 3.2.
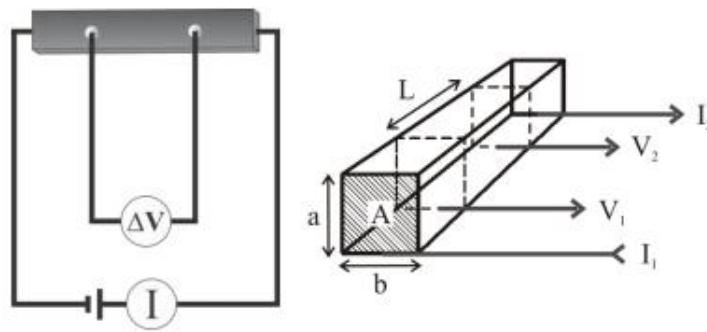
Figure 3.2 Four point probe method.

3.4.3 Hall effect measurements

Hall measurements were used to study charge carrier density in the conducting samples. In a typical Hall measurement, the magnetic field is applied perpendicular to the current direction. Under the magnetic field, the charge particles (electrons or holes) experience the force and move toward one side of the sample creating a potential difference called the Hall voltage (V_H). The carrier density can be calculated from the relation:

$$V_H = \frac{IB}{end} \tag{6}$$

I = Current (A)

V_H = Hall voltage (V)

B = Magnetic field (Wb/m^2 or T)

e = Electron charge (C/cm^2)

n = Carrier density (cm^{-3})

d = Sample thickness (mm)

In this work, charge carrier concentration was obtained by Hall measurement at room temperature using four-point probes in the van der Pauw configuration. The measurement system consists of Keithley 237 source measure unit, Keithley 196 digital multimeter, Agilent 34970 data acquisition, 34903A switching unit and 0.9 T electromagnet. All units and data acquisition are controlled by a personal computer.
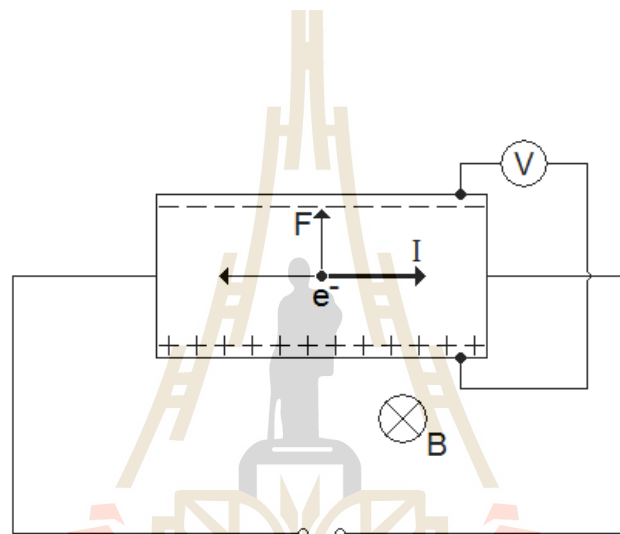
Figure 3.3 Schematic diagram of the Hall effect measurement.

3.5 References

Siritanon, T., Chathirat, N., Masingboon, C., Yamwong, T., and Maensiri, S. (2014). Synthesis, characterization, and dielectric properties of Y_2NiMnO_6 ceramics prepared by a simple thermal decomposition route. **J. Mater. Sci. - Mater. Electron.** 25: 1361-1368.

Smart, L.E. and Moore, E.A. (2005). **Solid state chemistry: An introduction** (3rd ed.). Boca Raton: Taylor & Francis group.

Tritt, T.M. and Subramanian, M.A. (2006). Thermoelectric materials, phenomena, and applications: a bird's eye view. **Mater. Res. Bull.** 31: 188-198.

CHAPTER IV

RESULTS AND DISCUSSION

4.1 Sample characterizations

4.1.1 Thermogravimetric analysis

Thermal decomposition of $Zn_{0.98}Al_{0.02}Mn_{0.02}O$ dried solution was investigated by the thermogravimetric analysis as shown in Figure 4.1. $Zn_{0.98}Al_{0.02}Mn_{0.02}O$ dried solution was used as a representative of all samples. TGA thermogram of the dried solution indicates that the sample thermally decomposes in two successive stages. The first step involving 5.45% weight loss at around 353 K is related to the loss of water molecules. The second stage in the temperature range 543-553 K is related to decomposition of acetate groups with weight loss of 44.12%. In the present case, this TGA thermogram is very similar to that of $Zn(CH_3COO)_2 \cdot 2H_2O$ which was used as a starting reagent. There are two stages of weight losses observed in TGA thermogram of $Zn(CH_3COO)_2 \cdot 2H_2O$. The first step observed at 353 K is corresponding to the thermal dehydration of two water molecules. The following mechanism of thermal decomposition can be proposed: $Zn(CH_3COO)_2 \cdot 2H_2O \rightarrow Zn(CH_3COO)_2 + 2H_2O$. After dehydration, the weight loss in the second step indicates the decomposition of anhydrous zinc acetate at 513 K (Ghule *et al*., 2003; 2004).

Theoretically, the first weight loss of $Zn(CH_3COOH)_2 \cdot 2H_2O$ should be 16.4% which is related to the loss of two water molecules to form anhydrous zinc acetate.

However, weight loss in the first stage of the dried solution sample in this case is only 5.45% because the dried solution sample was heated at 373 K for 5 hours prior to the thermal analysis. Anhydrous zinc acetate theoretically losses 46.5% weight in the second step which is close to the weight change observed in the sample. TGA shows that the stepwise thermal decomposition of the precursors completes at 623 K with the total weight loss of 47.57%. At temperature higher than 623 K, the weight remains constant indicating the complete decomposition of zinc acetate to form ZnO. This temperature was, therefore, chosen to use in the calcinations process.
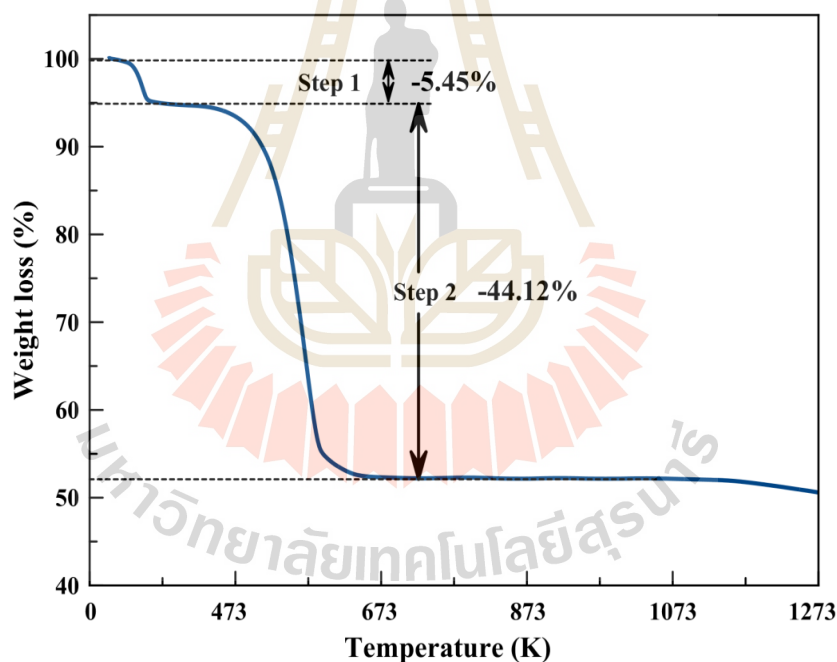

Figure 4.1 Thermogravimetric analysis of the $Zn_{0.92}Al_{0.04}Mn_{0.04}O$ dried solution.

4.2.2 Fourier transform infrared spectroscopy

Figure 4.2 shows the FT-IR spectra of dried solution, calcined, and sintered sample of $Zn_{0.92}Al_{0.04}Mn_{0.04}O$ synthesized by thermal decomposition method in the range of 400-4000 cm^{-1}. The observed peaks are assigned to vibrations of molecular bonds and indexed as shown in the figure. The FT-IR spectrum of dried solution shows similar functional groups characteristics to those observed in $Zn(CH_3COO)_2 \cdot 2H_2O$ starting material. The broad band around 3500 cm^{-1} is assigned to O-H stretching in water, while the absorption band around 1300-1450 cm^{-1} is assigned to stretching vibration of acetate group (COO^-). The present preparation method is different from the sol-gel method. Generally, the FT-IR spectrum of the gel in sol-gel method should be different from that of the stating materials (Tokumoto *et al*., 2003). In the present work, DMF solvent merely functions in homogenously mixing each cation in the atomic level which helps them to react easier to from products. Nevertheless, the thermal decomposition method has been proven successful in preparing many complex oxides at relatively low temperatures (Daengsakul *et al*., 2009; Labuayai *et al*., 2009; Nohman *et al*., 1995; Arof *et al*., 2008). The FT-IR spectrum of the calcined sample shows the evolution of the compound after a heat treatment at 623 K. The spectrum presents fewer absorption bands in the measured range indicating a much smaller amount of acetate groups. The absorption band around 3500 cm^{-1} corresponding to O-H stretching vibration of absorbed water from air and the acetate group (COO^-) stretching vibration bands around 1300-1450 cm^{-1} are still present in the cacined sample. However, the intensity of these bands decreases after calcinations and disappears when the sample is heated at high temperature. FT-IR spectrum of the sintered sample exhibits absorption bands around 400-600 cm^{-1}

which indicates the formation of oxides. These absorption bands at low wave numbers are characteristics of metal-oxygen bonds. The fact that only bands for metal-oxide bonds are present in the sintered sample indicates that all organic species have completely decomposed.
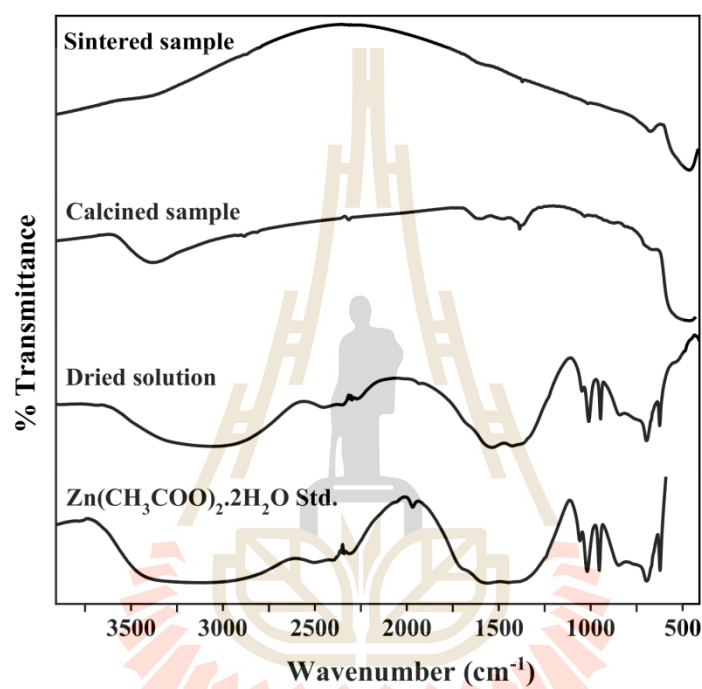
Figure 4.2 FT-IR spectra of $Zn(CH_3COO)_2 \cdot 2H_2O$, dried solution, calcined, and sintered sample of $Zn_{0.92}Al_{0.04}Mn_{0.04}O$.

4.2.3 X-ray diffraction

X-ray diffraction patterns of $Zn_{1-x}Al_xO$, $Zn_{1-x}Mn_xO$ (x = 0.02, 0.04, 0.06, 0.08), and $Zn_{1-2x}Al_xMn_xO$ (x = 0.01, 0.02, 0.03, 0.04) samples sintered at 1673 K are shown in Figure 4.3, 4.4, and 4.5, respectively. The XRD patterns reveal that the major phase has ZnO wurtzite structure with $P6_3mc$ space group in agreement with

the JCPDS data file No. 36-1451. For Al-doped ZnO samples, small peaks of the ZnAl$_2$O$_4$ spinel phase (JCPDS data file No. 5-0669), a second phase, can be observed. The intensity of ZnAl$_2$O$_4$ peaks increases with increasing the amount of Al. Values of Al solubility limit in ZnO are in between 0.3% to 4% (x = 0.003 to x = 0.04 in the formula) in literatures (Shirouzu *et al*., 2007; Lim *et al*., 2013; Ma *et al*., 2010). The difference is possibly a result of different preparation techniques. Although it is difficult to conclude the the exact solubility limit of Al in doped ZnO in this work, ZnAl$_2$O$_4$ phase is observed in the sample containing lower than 1% of Al, which confirms that the solubility limit of Al here is lower than 1%.

X-ray diffraction patterns for all Mn-doping levels show no secondary phase, indicating that the samples are all single phase. The XRD results indicate that all Mn ions replace Zn ions in the samples without changing the wurtzite structure. The results are consistent with the reported solubility limit of Mn in ZnO which is between 6% and 20% (x = 0.06 to x = 0.2 in the formula) (Riyadi *et al*., 2007; Deka *et al*., 2007). Furthermore, with increasing Mn doping level, the peak positions shift to lower angle. This indicates the changes of lattice parameters *a* and *c* (Å), both of which increase with increasing Mn content. XRD patterns of double substituted samples show the presence of the ZnO main phase and small amount of ZnAl$_2$O$_4$ spinel phase, similar to that of Al-doped samples.
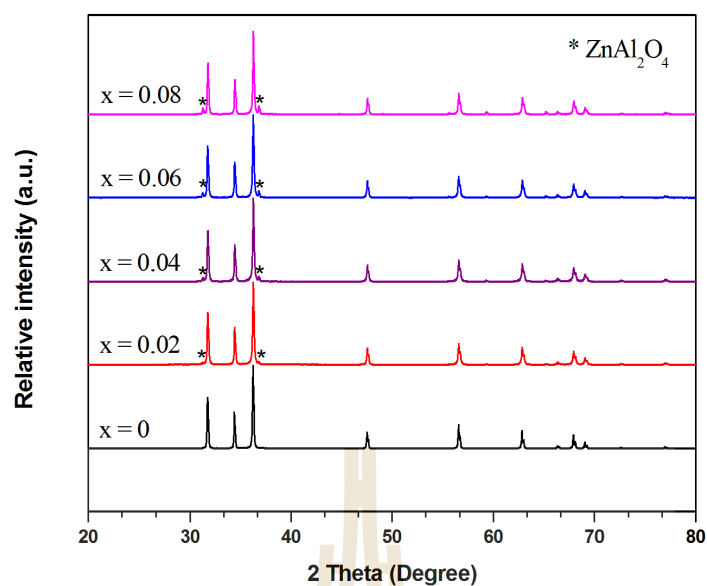
Figure 4.3 X-ray diffraction patterns of $Zn_{1-x}Al_xO$ (x = 0.02, 0.04, 0.06, 0.08) samples.
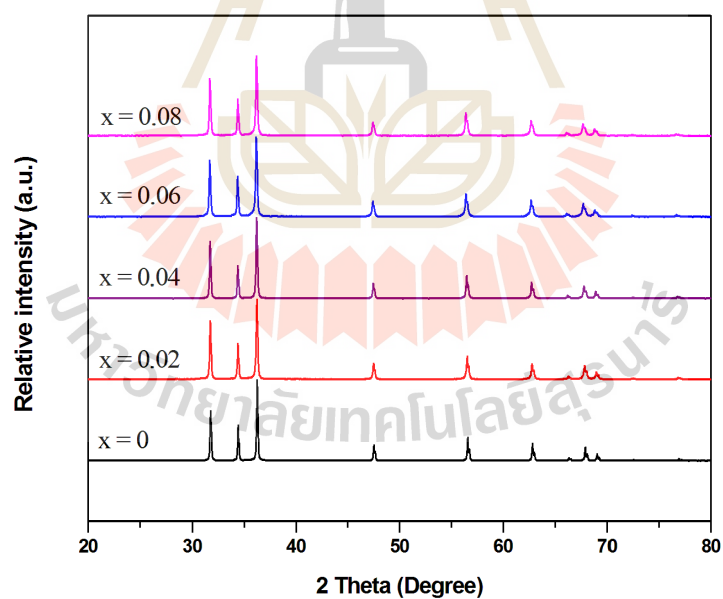
Figure 4.4 X-ray diffraction patterns of $Zn_{1-x}Mn_xO$ (x = 0.02, 0.04, 0.06, 0.08) samples.
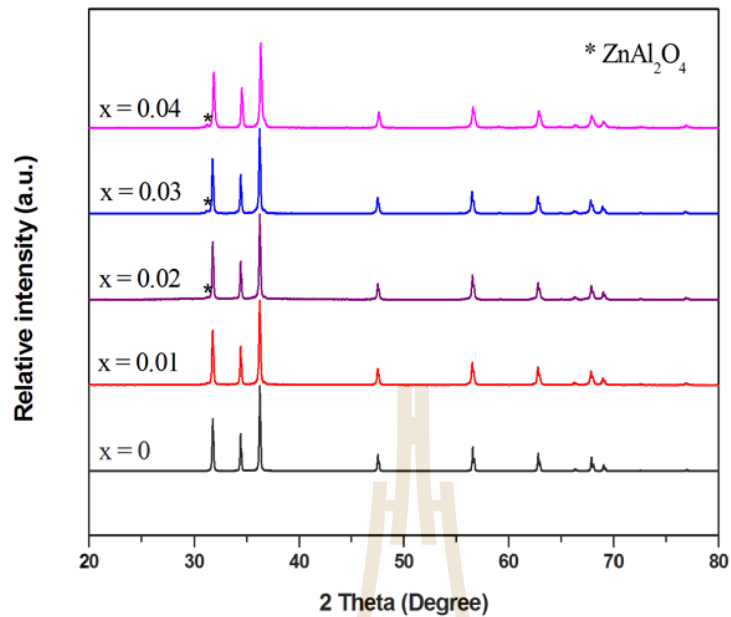
Figure 4.5 X-ray diffraction patterns of $Zn_{1-2x}Al_xMn_xO$ (x = 0.01, 0.02, 0.03, 0.04) samples.

Cell parameters of all samples were calculated using Le bail refinement method on TOPAS software (Table 4.1). The cell parameters *a* and *c* are plotted versus the doping content as shown in Figure 4.6. In general, the partial substitution of Al^{3+} in ZnO structure causes a decrease in unit cells because the ionic radii of Al^{3+} (0.39Å) is smaller than that of Zn^{2+} (0.60Å) in tetrahedral coordination (Shannon *et al*., 2013). However, the change of unit cells in Al-doped series is very small as only small amount of Al^{3+} is actually substituting Zn^{2+} ion while the rest appear in the form of secondary phase.

Replacing Mn in ZnO structure results in the larger unit cells. As Mn^{2+} (0.66 Å) is larger than that of Zn^{2+}, while both Mn^{3+} (0.64Å) and Mn^{4+} (0. 53Å) are

smaller, Mn in ZnO samples are most likely in 2+ state (Shannon *et al.*, 1976). The linear relation in Figure 4.6 also confirms that Mn solubility limit in this work has not been reached. Changes in cell parameters in co-doped series are in between the singly doped series as expected.
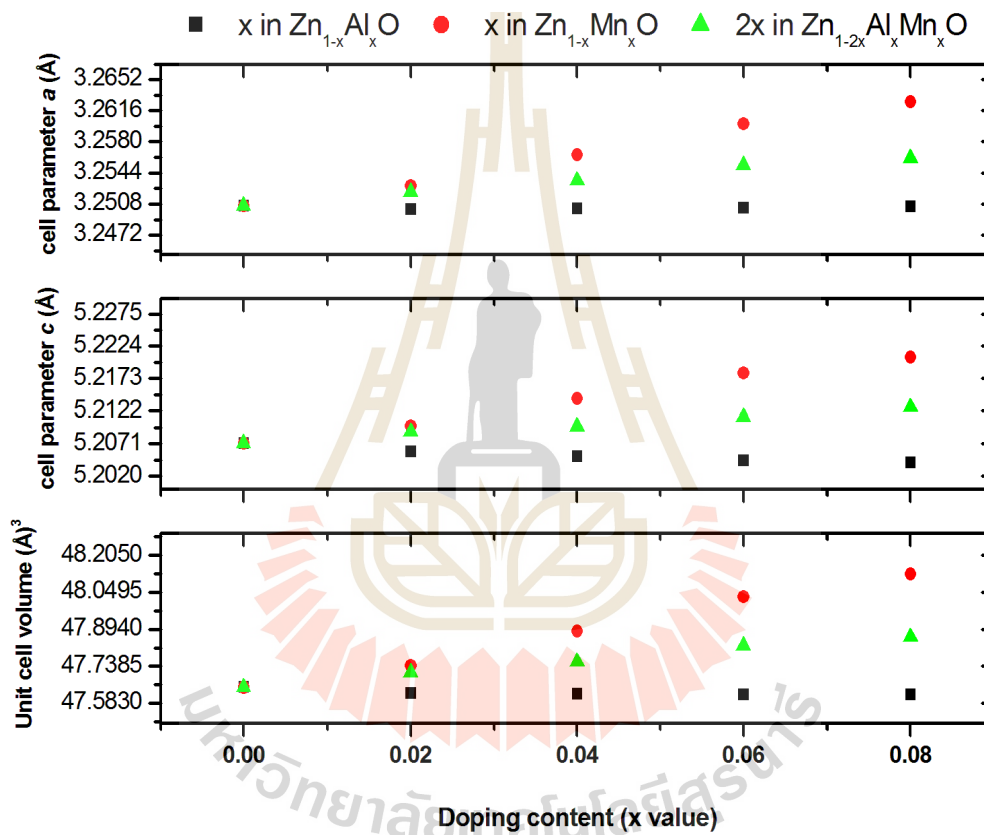
Figure 4.6 Cell parameters (a) *a* and (b) *c* and (c) the unit cell volume of $Zn_{1-x}Al_xO$, $Zn_{1-x}Mn_xO$ and, $Zn_{1-2x}Al_xMn_xO$.

Table 4.1 Cell parameters *a* and *c* of all samples calculated from TOPAS software
and the corresponding % Rwp.

Samples	a (Å)	c (Å)	% Rwp
ZnO	3.2506	5.2072	9.66
$Zn_{0.98}Al_{0.02}O$	3.2502	5.2059	9.76
$Zn_{0.96}Al_{0.04}O$	3.2503	5.2051	9.73
$Zn_{0.94}Al_{0.06}O$	3.2504	5.2045	8.54
$Zn_{0.92}Al_{0.08}O$	3.2505	5.2042	8.69
$Zn_{0.98}Mn_{0.02}O$	3.2529	5.2099	9.73
$Zn_{0.96}Mn_{0.04}O$	3.2565	5.2141	7.92
$Zn_{0.94}Mn_{0.06}O$	3.2601	5.2182	8.96
$Zn_{0.92}Mn_{0.08}O$	3.2626	5.2207	8.60
$Zn_{0.98}Al_{0.01}Mn_{0.01}O$	3.2522	5.2090	8.43
$Zn_{0.96}Al_{0.02}Mn_{0.02}O$	3.2535	5.2098	8.94
$Zn_{0.94}Al_{0.03}Mn_{0.03}O$	3.2553	5.2113	9.64
$Zn_{0.92}Al_{0.04}Mn_{0.04}O$	3.2561	5.2128	8.40

4.2.4 X-ray Absorption Spectroscopy

Mn oxidation states in Mn-doped ZnO and co-doped ZnO samples were investigated by X-ray absorption near edge structure (XANES). Normalized XANES spectra at Mn K-edge of the Mn-doped ZnO samples along with standard compounds; MnO, Mn_2O_3, and MnO_2, are shown in Figure 4.7. Edge energy (summarized in table 4.2) and spectra feature of the standards are similar to those reported in literatures (Zhang *et al*., 2013; Yadav *et al*., 2015). Edge energy of the samples (green dash line) is close to that of MnO (red dash line) but slightly shifted toward Mn_2O_3 (blue dash line), as can be seen in Figure 4.7b. The slight shift of edge energy might be a result of structural factors rather than oxidation state (Zhang *et al*., 2013; Fages *et al*., 2005; Mini *et al*., 1997). It is therefore concluded that Mn in Mn-doped ZnO was mainly in 2+ oxidation state. Although it is difficult to judge the oxidation state of manganese in Mn-doped ZnO samples based solely on the edge position, the continue shift of edge energy from sample with x = 0.02 to x = 0.08 led us to believe that there possibly be small amount of Mn with oxidation state higher than 2+ in the samples as well. The pre-edge peaks as shown in Figure 4.7c are related to the transition of Mn 1s electrons to unoccupied states above the Fermi level and their high intensity as observed here suggests that Mn is in tetrahedral environment (Mini *et al*., 1997) which confirms the presence of Mn in wurtzite structure. Additionally, for structure with tetrahedral coordination, the single pre-edge peak is also an indicative of Mn^{2+} species as Mn^{3+} will give rise to two pre-edge peaks (Titov *et al*., 2005).
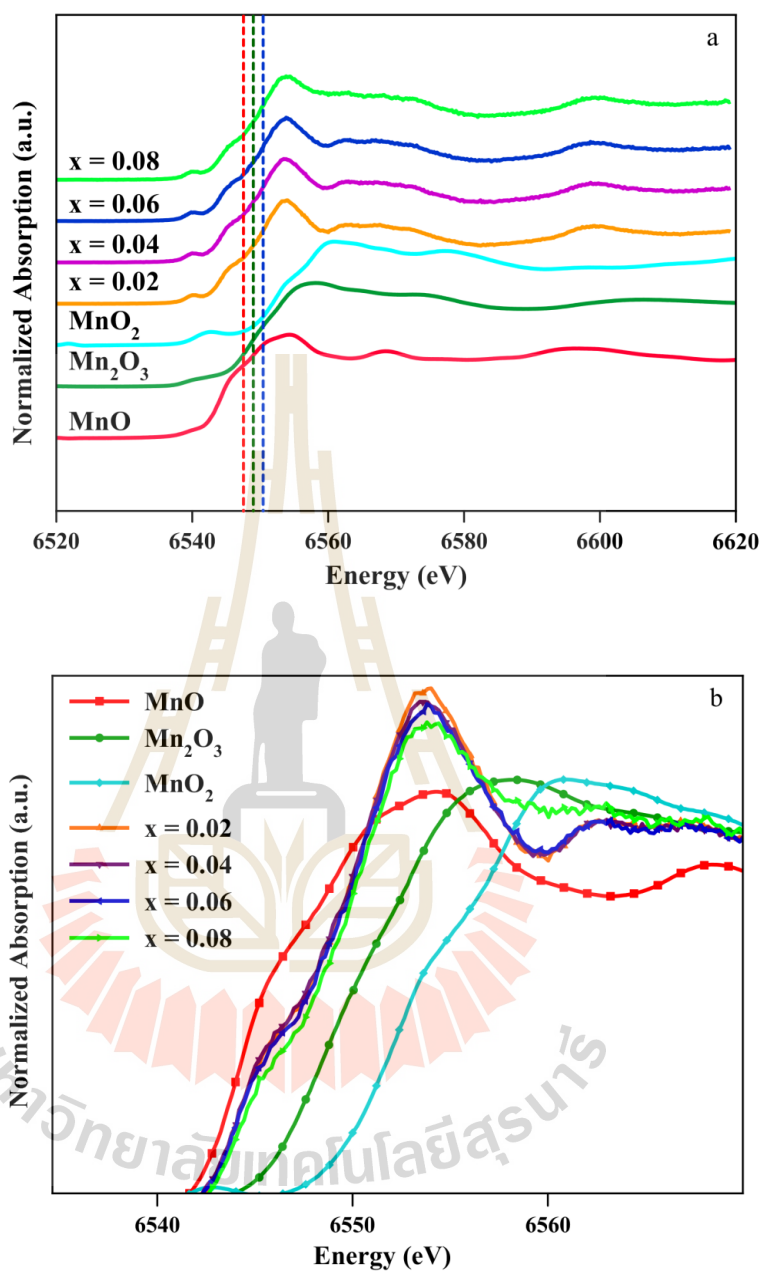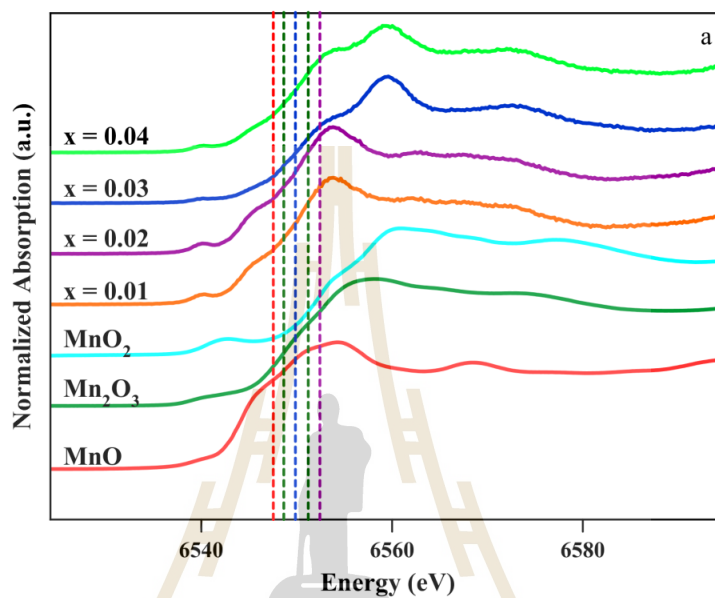
Figure 4.7 (a,b) Normalized K-edge XANES spectra of $Zn_{1-x}Mn_xO$ (x = 0.02, 0.04, 0.06, 0.08) samples and manganese oxide standards, (c) Pre-edge spectra.
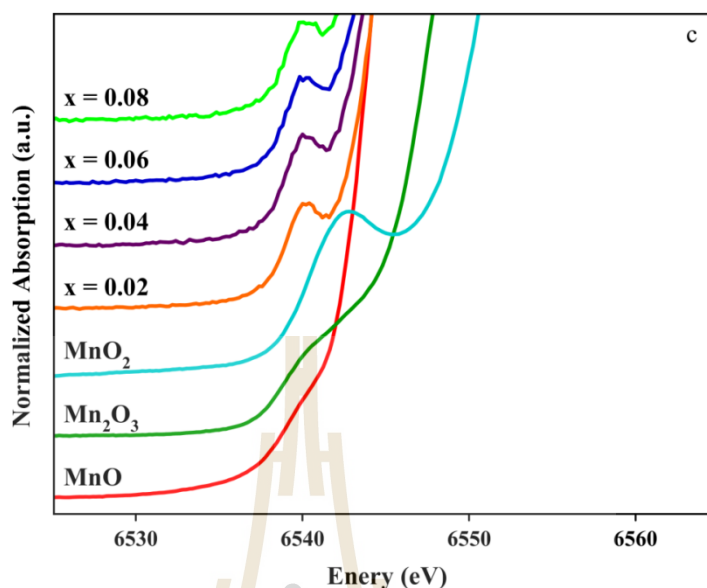
Figure 4.7 (a,b) Normalized K-edge XANES spectra of $Zn_{1-x}Mn_xO$ (x = 0.02, 0.04, 0.06, 0.08) samples and manganese oxide standards, (c) Pre-edge spectra (Continued).

Normalized Mn K-edge XANES spectra of x = 0.01 and x = 0.02 co-doped samples (green dash line) as shown in Figure 4.8a are similar to those of Mn-doped samples indicating the presence of Mn^{2+} in ZnO lattice. However, edge energy of the spectra for x = 0.03 and x = 0.04 co-doped samples (green dash line) clearly shift and are closer to that of Mn_2O_3 (blue dash line) and MnO_2 standard (purple dash line). Thus Mn in these two samples are in 3+ and possibly mixed 3+/4+ states. As the spectral feature of these samples is different from that of Mn_2O_3 and MnO_2 standard, these two samples should not contain neither oxides as impurity. The absence of other impurity peaks in the XRD patterns also indicates that Mn^{3+} and Mn^{4+} in these samples might also be in the wurtzite lattice. However, other possibility is that they

form impurity phases which are either too small in quantity or are not crystalline enough to be detected by XRD. Further studies are required to clarify this matter.

Figure 4.8 (a,b) Normalized K-edge XANES spectra of $Zn_{1-2x}Al_xMn_xO$ (x = 0.01, 0.02, 0.03, 0.04) samples and manganese oxide standards, (c) Pre-edge spectra.

Figure 4.8 (a,b) Normalized K-edge XANES spectra of $Zn_{1-2x}Al_xMn_xO$ (x = 0.01, 0.02, 0.03, 0.04) samples and manganese oxide standards, (c) Pre-edge spectra (Continued).

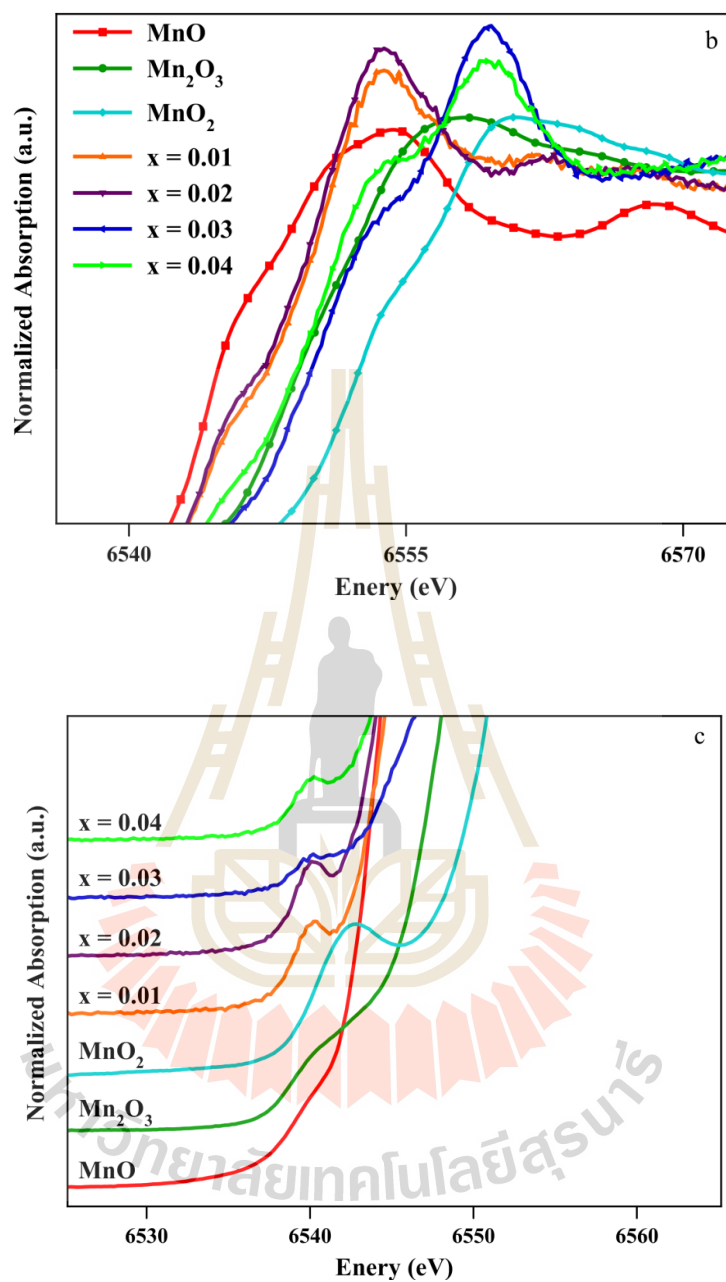**Table 4.2** Edge energy at Mn K-edge of Mn doped samples and the standard

compounds.

Samples	Edge energy (eV)
MnO	6544
Mn_2O_3	6549
MnO_2	6552
$Zn_{0.98}Mn_{0.02}O$	6544
$Zn_{0.96}Mn_{0.04}O$	6544
$Zn_{0.94}Mn_{0.06}O$	6544
$Zn_{0.92}Mn_{0.08}O$	6544
$Zn_{0.98}Al_{0.01}Mn_{0.01}O$	6544
$Zn_{0.96}Al_{0.02}Mn_{0.02}O$	6544
$Zn_{0.94}Al_{0.03}Mn_{0.03}O$	6550
$Zn_{0.92}Al_{0.04}Mn_{0.04}O$	6548

4.2.5 Scanning Electron Microscopy / Energy Dispersive Spectroscopy

Substituting Al and Mn in ZnO does have some effects on the sample

morphology as shown in Figure 4.9. The grain size as observed from SEM images of

Al containing sintered samples are in the range of few microns. The sample with

higher Al content seems to have slightly smaller grain size (Figure 4.9b) which is a

result of the pining effect (Bérardan *et al*., 2010). The inhomogeneity of these samples

is clear as they contain several small precipitates. EDS results indicate that majority of

the samples are Al-substituted ZnO while the precipitates are Al rich, most probably $ZnAl_2O_4$ phase, which is also observed in XRD patterns. On the other hand, doping Mn increases grain size of the sample. Han *et al*. (2001) suggested that Mn exists in the grain boundary and promotes the grain growth by forming the continuous grain boundary phases which increase mass diffusion during the growth. Comparing to Al, Mn distributes much better in the sintered pellet although some Mn-rich regions are still present in samples with higher Mn content as shown in Figure 4.9d. The contrast between Al and Mn distribution in the samples is clearly observed in Figure 4.10 where only Al-rich precipitates are present. Our results are different from those recently reported by Hoemke *et al*. (2016) who prepared similar samples with formula $Zn_{0.9-x}Mn_xAl_{0.01}O$ (x = 0.01, 0.02, 0.05, 0.1) and found Mn-rich precipitates in both grains and grain boundary region. The major differences between these two sets of samples are the preparation method. The thermal decomposition route used in this work might play important roles in obtaining more homogeneous samples.
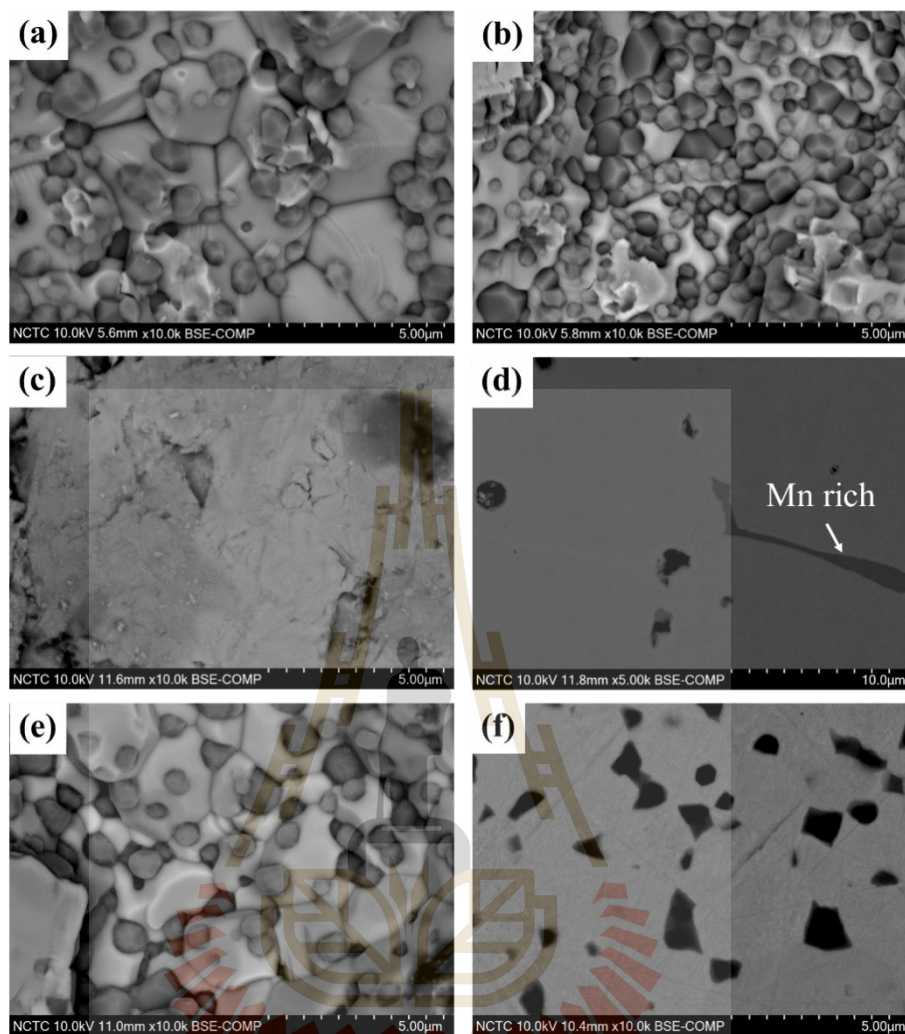
Figure 4.9 SEM images of $Zn_{0.98}Al_{0.02}O$ (a), $Zn_{0.92}Al_{0.08}O$ (b), $Zn_{0.98}Mn_{0.02}O$ (c), $Zn_{0.92}Mn_{0.08}O$ (d), $Zn_{0.98}Al_{0.01}Mn_{0.01}O$ (e), and $Zn_{0.92}Al_{0.04}Mn_{0.04}O$ (f).
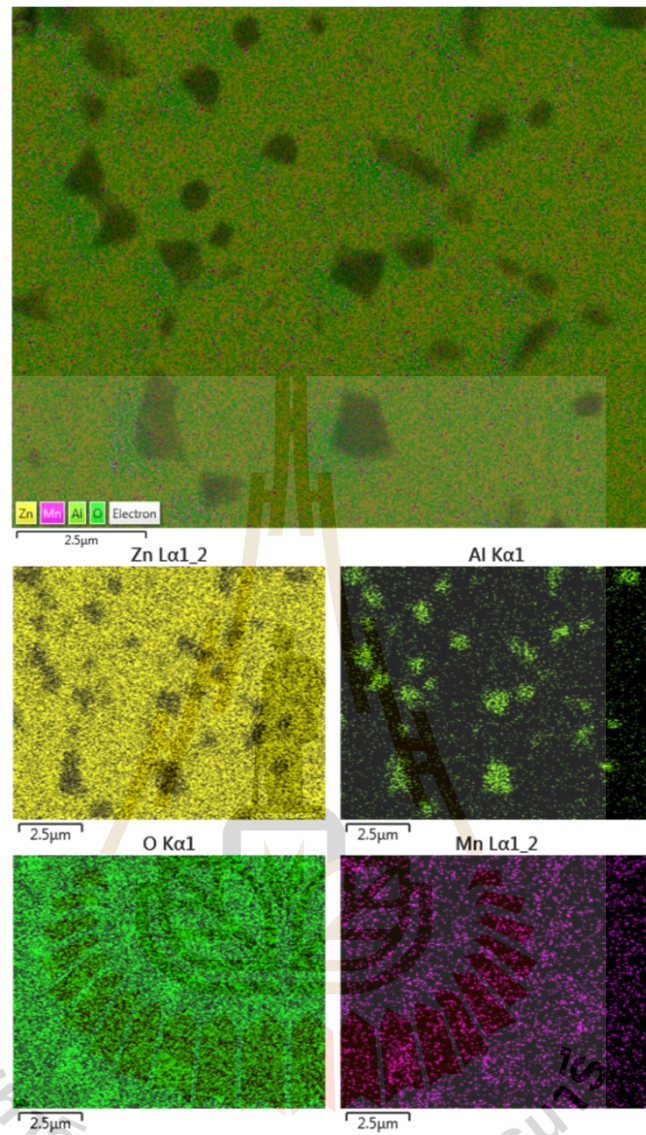
Figure 4.10 EDS elemental mapping of $Zn_{0.92}Al_{0.04}Mn_{0.04}O$ sintered sample.

4.3 Thermoelectric properties

4.3.1 Electrical resistivity

The electrical resistivity of all samples are shown in Figure 4.11. Substituting small amount of Al (2% and 4%) results in a significant decrease in resistivity. In general, resistivity is related to carrier concentration (n) and carrier mobility (μ) through $1/\rho = ne\mu$ when e is electrical charge (1.602×10^{-19} C) (Snyder and Toberer, 2008). Substituting Zn^{2+} by Al^{3+} add one extra electron into the system since Al atom have three valence electrons while Zn atom has only two valence electrons. Adding Al adds the donor levels to the band structure. This extra electron is excited from donor energy levels to conduction band which increases the electrical conductivity in the sample and consequently causes a reduction in its electrical resistivity. Generally, Al dopant is well known to act as a donor and can improve the electrical conductivity of ZnO. However, higher Al content in ZnO increase electrical resistivity because the low solubility limit of Al in ZnO gives rise to the insulating impurity phase whose presence increases the resistivity. Therefore, increasing Al content results in the increased resistivity and samples with higher Al content only show semiconducting behavior whereas $Zn_{0.98}Al_{0.02}O$ and $Zn_{0.98}Al_{0.01}Mn_{0.01}O$ exhibit metallic behavior. While electrical property of Al doped ZnO is well established with several reports in literatures (Jantrasee *et al*., 2014; Qu *et al*., 2011), the reports on Mn doped ZnO are inconsistent. In this works, the doped samples had much higher resistivity than the undoped one. All Mn singly doped samples show semiconducting behavior. In fact, the conductivity of the samples at lower temperatures was very small and could not be measured with the current technique. Hall measurements at room temperature indicate that Mn^{2+} decreases carrier concentration of samples.

While carrier concentration of $Zn_{0.98}Al_{0.02}O$ is as high as 1.5×10^{19} cm^{-3}, that of $Zn_{0.96}Al_{0.02}Mn_{0.02}O$ is only at 9.4×10^{17} cm^{-3}. Many studies indicate that substituting Mn^{2+} increase resistivity of ZnO because Mn acts as a deep donor and suppress the intrinsic defects which are usually responsible for the conduction in ZnO (Motevalizadeh *et al.*, 2016; Shinde *et al.*, 2006; Han *et al.*, 2002; Tuomisto *et al.*, 2006; Plugaru *et al.*, 2012). On the other hands, some works reported the slight decreased resistivity in Mn-doped ZnO (Chvostova *et al.*, 2011; Wu *et al.*, 2010). Cao *et al.* (2004) suggested, based on XPS results, that Mn^{2+} in the structure capture oxygen and create more oxygen vacancies which contribute to the conduction. In addition, Hoemke *et al.* (2013) who prepared the very similar samples have concluded, based on the Seebeck coefficients, that Mn is a neutral impurity and do not affect carrier concentration in ZnO. It should be noted that both the preparation and measurement conditions have effects on the obtained results and might be one reason of the inconsistency (Cao *et al.*, 2004; Abrishami *et al.*, 2012). The different resistivity observed in samples with different Mn content was very small and could be caused by the presence of Mn^{3+} as observed in XAS results or the sample microstructure. Resistivity of the co-doped samples can be explained based on the coexisting effects from both Al and Mn substitutions which result in the increased resistivity when the doping content is increased.
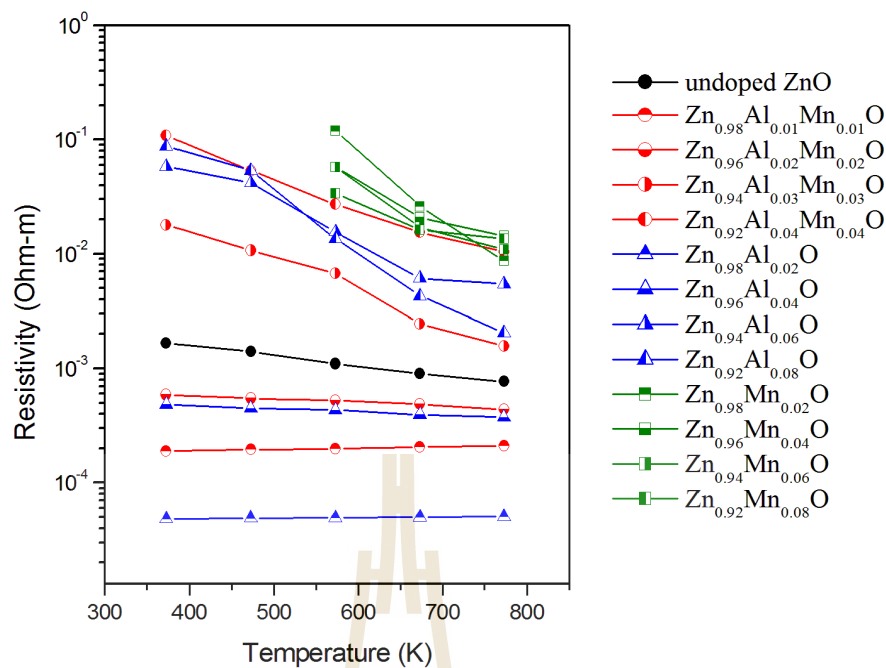
Figure 4.11 The resistivity of all samples at various temperatures.

4.3.2 Seebeck coefficient

The Seebeck coefficients (S) of all samples are shown in Figure 4.12. All substituted ZnO samples show negative Seebeck coefficient indicating that the main charge carriers are electrons. In general, Seebeck coefficient is strongly correlated to the electrical conductivity of the samples and samples with low resistivity usually have low absolute value of Seebeck coefficient. Deviation from this correlation was reported in doped ZnO system but the reasons are still unclear (Yanagiya *et al*., 2010; Park *et al*., 2008; Colder *et al*., 2011). Al substitution decreases the Seebeck coefficient of ZnO because it increases carrier concentration of the system. However, Absolute Seebeck coefficient, $|S|$, of Al-doped ZnO samples increase with Al

content which is a result of impurity. The Seebeck coefficient of Mn-doped ZnO thin film has been studied experimentally and theoretically by (Ghosh *et al.*, 2007) who suggested that the unfilled Mn d orbital in cause the unbalance spin up and spin down electrons in the conduction band enhancing the Seebeck coefficient. The Seebeck coefficient enhancement in Mn doped ZnO is also obvious in this work though the relationship between the value and Mn content is not as clear. Absolute Seebeck coefficient of the co-doped samples increases with increasing doping content, which is consistent with the observed trend in electronic resistivity. However, $Zn_{0.94}Al_{0.03}Mn_{0.03}O$ and $Zn_{0.92}Al_{0.04}Mn_{0.04}O$ samples show unexpectedly low absolute value of Seebeck coefficient indicating that the same explanation on the effects of Mn^{2+} on Seebeck coefficient of ZnO could not be applied with the samples with Mn^{3+} and/or mixed Mn^{3+}/Mn^{4+}.
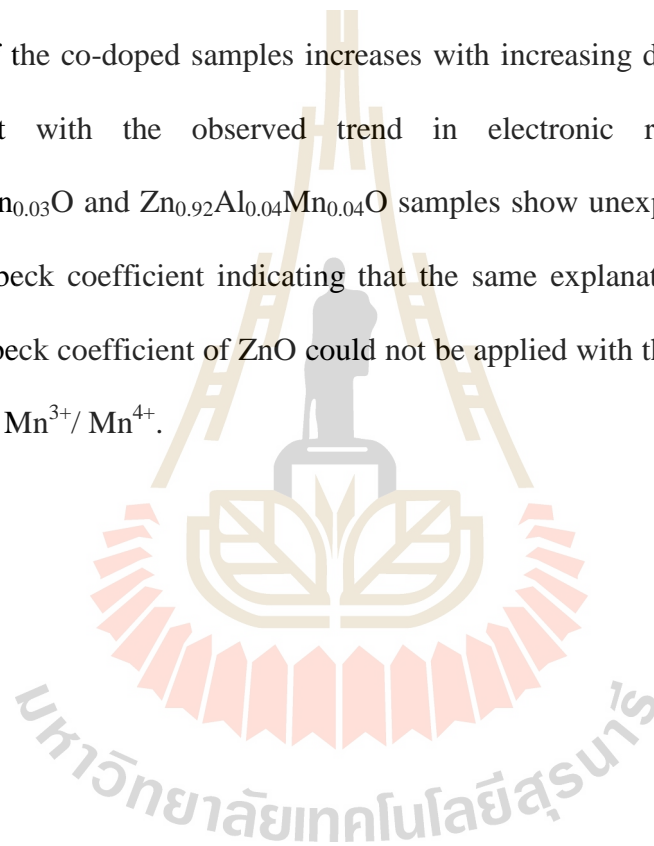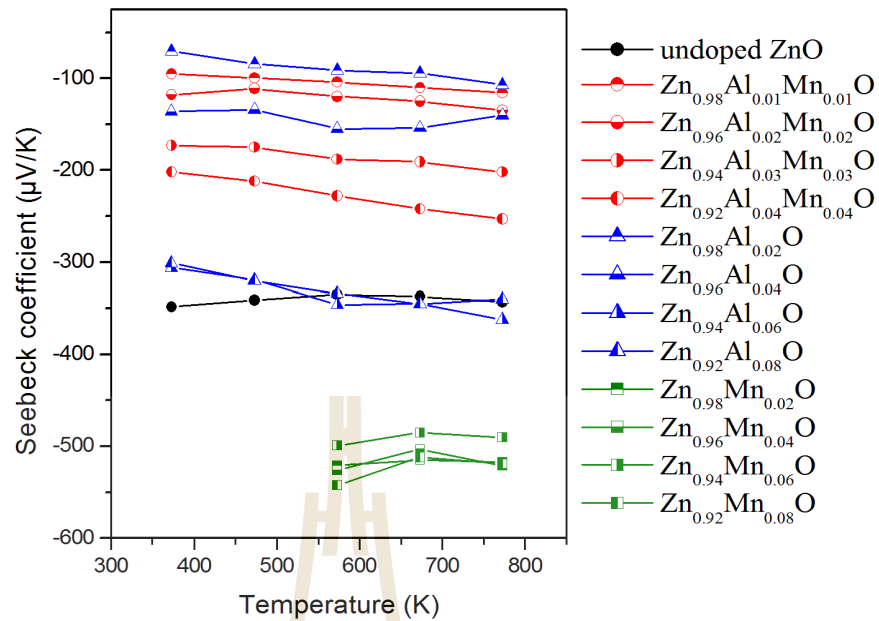
Figure 4.12 Seebeck coefficients of all samples at various temperatures.

4.3.3 Power factor

Power factor of the obtained samples are calculated from $(1/\rho)S^2$ (WK^{-2}m^{-1}) and summarized in Figure 4.13. Both electrical resistivity and Seebeck coefficient affect the power factor. However, the high power factor is obtained mainly from the samples with low resistivity regardless of their low absolute Seebeck coefficients. Among all samples prepared in this work, the highest value of power factor of 1.03×10^{-4} WK^{-2}m^{-1} at 773 K is achieved in $Zn_{0.98}Al_{0.02}O$ which exhibits the lowest resistivity. The best double substituted sample is $Zn_{0.98}Mn_{0.01}Al_{0.01}O$ which gives a power factor of 4.79×10^{-5} WK^{-2}m^{-1} at the same temperature.
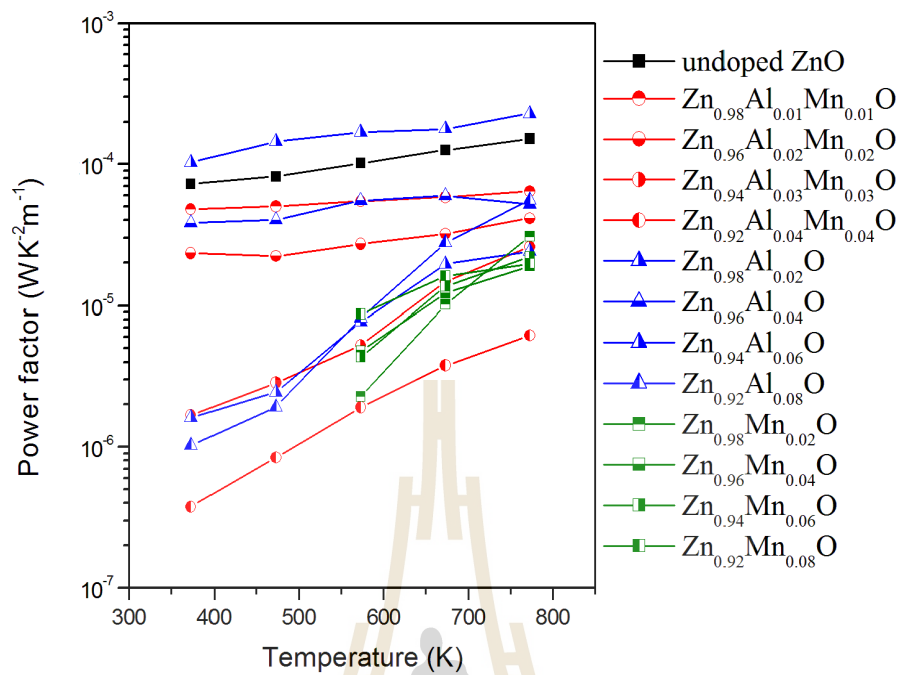
Figure 4.13 Power factor of all samples various temperatures.

4.4 References

Abrishami, M.E., Kompany, A., Hosseini, S.M., and Bardar, N.G. (2012). Preparing undoped and Mn-doped ZnO nanparticles: a comparison between sol-gel and gel-combustion methods. **J. Sol-Gel Sci. Techn.** 62: 153-159.

Arof, A.K. (2008). Characteristics of $LiMO_2$ (M= Co, Ni, $Ci_{0.2}Co_{0.8}$, $Ni_{0.8}Co_{0.2}$) powders prepared from solution of their acetates. **J. Alloy. Compd.** 449: 288-291.

Béradan, D., Célin, B.D., and Dragoe, N. (2010). Influence of the preparation conditions on the thermoelectric properties of Al-doped ZnO. **J. Am. Ceram. Soc.** 93: 2352-2358.

Cao, H.T., Pei, Z.L., Gong, J., Sun, C., Huang, R.F., and Wen, L.S. (2004). Preparation and characterization of Al and Mn doped ZnO (ZnO:(Al,Mn)) transparent conducting oxide films. **J. Solid State Chem.** 177: 1480-1487.

Chvostova, D., Dejneka, A., Hubicka, Z., Churpita, A., Bykov, P., Jastrabik, L., and Trepakov, V.A. (2011). Synthesis and optical properties of Mn doped ZnO thin films. **Phys. Status Solidi A.** 208: 2140-2143.

Colder, H., Guilmeau, E., Harnois, C., Marinel, S., Retoux, R., and Savary, E. (2011). Preparation of Ni-doped ZnO ceramic for thermoelectric applications. **J. Eur. Ceram. Soc.** 31: 2957-2963.

Daengsakul, S., Mongkolkachit, C., Thomas, C., Siri, S., Thomas, I., Amornkitbamrung, V., and Maensiri, S. (2009). A simple thermal decomposition synthesis, magnetic properties, and cytotoxicity of $La_{0.7}Sr_{0.3}MnO_3$ nanoparticles. **Appl. Phys. A.** 96: 691-699.

Deka, S., and Joy, P.A. (2007). Synthesis and magnetic properties of Mn doped ZnO nanowire. **Solid State Commun.** 142: 190-194.

Farges, F. (2005). Ab initio and experiment pre-edge investigationsnof the Mn K-edge XANES in oxide-type materials. **Phys. Rev. B.** 71: 155109.

Ghosh, C.K., Das, S., and Chattopadhyay, K.K. (2007). Enhancement of thermopower of Mn doped ZnO thin film. **Physica B.** 399: 38-46.

Ghule, A.V., Ghule, K., Chen, C-Y., Chen, W-Y., Tzing, S-H., Chang, H., and Ling, Y-C. (2004). In situ thermo-TOF_SIMS study of thermal decomposition of zinc acateate dehydrate. **J. Mass Spectrom.** 39: 1202-1208.

Ghule, A.V., Lo, B., Tzing, S-H., Ghule, K., Chang, H., and Ling, C.Y. (2003). Simulataneous thermogravimetric analysis and in situ thermo-Raman spectroscopic investigation of thermal decomposition of zinc acetate dehydrate forming zinc oxide nanoparticles. **Chem. Phys. Lett.** 381: 262-270.

Han, J., Matas, P.Q., and Senos, A.M.R. (2000). Efect of Al amd Mn doping on the thermoelectric conductivity of ZnO. **J. Eur. Ceram. Soc.** 21: 183-1886.

Han, J., Mantas, P.Q., and Senos, A.M.R. (2001). Effect of Al and Mn doping on the electrical conductivity of ZnO. **J. Eur. Ceram. Soc.** 21: 1883-1886.

Han, J., Mantas, P.Q., and Senos, A.M.R. (2002). Defect chemistry and electrical charecteristics of undoped and Mn-doped ZnO. **J. Eur. Ceram. Soc.** 22: 49-59.

Han, L., Nong, N.V., Hung, L.T., Holgate, T., Pryds, N., and Ohtaki, M. (2013). The influence of α-and γ-Al_2O_3 phases on the thermoelectric properties of Al-doped ZnO. **J. Alloy. Compd.** 555: 291-296.

Hoemke, J., Khan, A.U., Ypshida, H., Mori, T., Tochigi, E., Shibata, N., Ikuhara, Y., and Sakka, Y. (2016). Sintering charecteristics and thermoelectric properties of Mn-Al co-doped ZnO ceramics. **J. Ceram. Soc. Jpn.** 124: 515-522.

Jantrasee, S., Pinitsoontorn, S., and Moontragoon, P. (2014). First-principle study of the electronic structure and thermoelectric properties of Al-doped ZnO. **J. Electon. Mater.** 43: 1689-1695.

Labuayai, S., Promarak, V., and Meansiri, S. (2009). Synthesis and optical properties of nanocrystalline ZnO powders prepared by a direct thermal decomposition route. **Appl. Phys. A.** 94: 755-761.

Lim, L.H., Yeoh, C.K., The, P.L., Chik, A., and Arif, W.M. (2013). Effect of Al doping concentration to the physical and thermoelectric properties of zinc oxide. **Aust. J. Basic Appl. Sci.** 5: 21-23.

Ma, N., Li, J.-F., Zhang, B.P., Lin, Y.H., Ren, L.R., and Chen, G.F. (2010). Microstructure and thermoelectric properties of $Zn_{1-x}Al_xO$ ceramic fabricated by spark plasma sintering. **J. Phys. Chem.** 71: 1344-1349.

Mini, M.S., Mitchell, F.J., Hinks, D.G., Rosenmann, S., Kimball, C.W., and Montano, P.A. (1007). Mn K-edge x-ray absorption spectroscopy (XAS) studies of $La_{1-x}Sr_xMnO$. **MAS Proc.** 494: 59.

Motevalizadeh, L., Shohany, B.G., and Abrishami, M.E. (2016). Effects on Mn doping on electrical properties of ZnO thin films. **Phys. Lett. B.** 30: 1650024.

Nohman, A.K.H., Ismail, H.M., and Hussein, G.A.M. (1995). Thermal and chemical events in the decomposition course of manganese compounds. **J. Anal. Appl. Pyrolysis.** 34: 265-278.

Park, K., Seong, J.K., and Nahm, S. (2008). Improvement of thermoelectric properties with the addition of Sb to ZnO. **J. Alloy. Compd.** 455: 331-335.

Plugaru, R., Sandu, T., and Plugaru, N. (2012). First principles and variable rang hopping conductivity in disordered Al/Ti/Mn-doped ZnO. **Results Phys.** 2: 190-197.

Qu, X., Wang, W., Lv, S., and Jia, D. (2011). Thermoelectric properties and electronic structure of Al-doped ZnO. **Solid State Commun.** 151: 332-336.

Riyadi, S., Muafif, A.A., Nugroho, A., Rusydi, A., and Tjia, M.O. (2007). Mn-dopant-induced effects in $Zn_{1-x}Mn_xO$ compounds. **J. Phys. Condens. Matter.** 19: 476214 (8pp).

Shannon, R.D. (1976). Revised effective ionic radii and systematic studies of interatomic distances in halides and chalcogenides. **Acta Crystallogr. Sect. A.** 32: 751-767.

Shinde, V.R., Gujar, T.P., Lokhande, C.D., Mane, R.S., and Han, S.-H. (2006). Mn doped and undoped ZnO films:A comparative structure optical and electrical properties study. **Mater. Chem. Phys.** 96: 326-330.

Shirouzu, K., Ohkusa, T., Hotta, M., Enomoto, N., and Hojo, J. (2007). Distribution and solubility limit of Al in Al_2O_3-doped ZnI sintered body. **J. Ceram. Soc. Jpn.** 115: 254-258.

Snyder G.J. and Toberer E.S. (2008).Complex thermoelectric materials. **Nanostruct. Mater.** 7: 105-114.

Titov, A., Biquard, X., Halley, D., Kuroda, S., Bellet-amalric, E., Mariette, H., Cibert, J., and Merad, A.E. (2005). X-ray absorption near-edge structure and valence state of Mn in (Ga, Mn) N. **Phys. Rev. B.** 72: 115209.

Tokumoto, M.S. (2003). Preparation of ZnO nanoparticales: Structure study of the molecular precursor. **J. Sol-Gel Sci. Techn.** 26: 547-551.

Tuomisto, F., Saarinen, K., and Grasza, K. (2006). Observation of ZnO by chemical vapor transport. **Phys. Status Solidi B.** 243: 794-798.

Wu, D., Huang, Z., Yin, G., Yao, Y., Liao, x., Han, D., Huang, X., and Gu, J. (2010).
Preparation, structure and properties of Mn-doped ZnO rod arrays. **Cryst.
Eng. Commun.** 12: 192-198.

Yadav, A.K., Haque, S.M., Shukla, D., Choudhary, R.J., Jha, S.N., and
Bhattacharyya, D. (2015). X-ray absorption spectroscopy of Mn doped ZnO
thin films prepared by rf sputtering technique. **AIP Advances.** 5: 117138-
17.

Yanagiya, S.-I., Nong, N. V., Xu, J., and Pryds, N. (2010). The effect of (Ag, Ni, Zn)
addition on the thermoelectric properties of copper aluminate. **Mater.** 3:
318-328.

Zhang, B., Li, M., Wang, J.Z., Shi, L.Q., and Cheng, H.S. (2013). XANES and XPS
study on microstructure of Mn-doped ZnO films. **Mater. Sci. Appl.** 4: 307-
311.

Zhao, Y., Kumar, A., Khodaparast, G.A., Eltahir, A., Wang, H., and Priya, S. (2014).
Sintering temperatuture-dependent chemical defects and effect on the
electrical resistivity of ZnO. **Energy Harvesting and Systems.** 1: 113-119.

CHAPTER V

CONCLUSIONS

In this thesis, series of Al and Mn single and double substituted ZnO have been prepared by thermal decomposition method where a solution of stoichiometric mixtures of metal acetate and nitrate is directly heated. Structural characterization by X-ray diffraction suggests that substituting Al and Mn does not change the structure of ZnO. However, the low solubility limit of Al results in a presence of $ZnAl_2O_4$ secondary phase which can be clearly observed as small precipitates in SEM images. On the other hand, there is no indication of any secondary phase or clusters in all Mn-substituted samples. Changes in lattice parameters and Mn K-edge XANES suggest that Mn is mainly 2+ state in Mn doped ZnO but evidence of Mn^{3+} and Mn^{4+} existence was observed in 3% and 4% double substituted samples. Thermoelectric properties of all samples have been investigated. Electrical conductivity of ZnO is improved by Al substitution while the Seebeck coefficient is significantly improved by Mn substitution. Double substituted samples seem to show effects from both Al and Mn. Nevertheless, the effect of electrical conductivity is dominant. Among all samples prepared in this work, that with 2% Al exhibits the lowest resistivity thus the highest power factor followed by ZnO and 1% double substituted sample, respectively.

APPENDICES
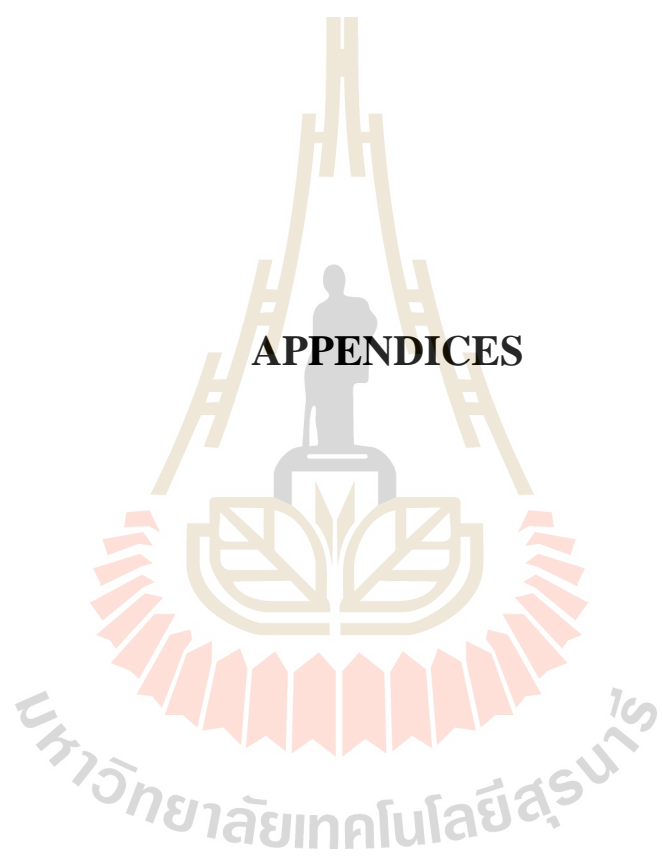
APPENDIX A

CALCULATION: A SAMPLE PREPARATION

A.1 Calculation of a sample preparation

Samples of $Zn_{1-x}Al_xO$, $Zn_{1-x}Mn_xO$ (x = 0.02, 0.04, 0.06, 0.08), and $Zn_{1-2x}Al_xMn_xO$ (x = 0.01, 0.02, 0.03, 0.04) were prepared by weighting starting materials in a stoichiometric ratio. The calculation procedure is as following;

Firstly, the number of mol of a sample is calculated using molecular weight (M.W.) of a sample.

mol of a sample　　　　　= (gram of a sample)/(M.W. of a sample)

Secondly, a weight of each precursor is calculated using its M.W. mol of a sample (from the first step), and mol of an atom (in a formula).

weight of a precursor　= (M.W. of a precursor) × (mol of a sample) × (mol of

an atom)

For example, 1 gram of $Zn_{0.98}Al_{0.02}O$ can be prepared by following calculations;

mol of $Zn_{0.98}Al_{0.02}O$　　　　= 1 g/(80.62 g/mol)

　　　　　　　　　　　　　= 0.0124035 mol

weight of $Zn(CH_3COO)_2 \cdot 2H_2O$ = 219.5098 g/mol × (0.0124035 × 0.98 mol)

　　　　　　　　　　　　　= 2.6682 g

weight of $Al(NO_3)_2 \cdot 9H_2O$　　= 375.13 g/mol × (0.01240359 × 0.02 mol)

　　　　　　　　　　　　　= 0.0906 g

For example, 1 gram of $Zn_{0.98}Mn_{0.02}O$ can be prepared by following calculations;

mol of $Zn_{0.98}Mn_{0.02}O$ = 1 g/(81.198 g/mol)

                                           = 0.012315574 mol

weight of $Zn(CH_3COO)_2 \cdot 2H_2O$ = 219.50 g/mol $\times$ (0.012315574 $\times$ 0.98 mol)

                                           = 2.6493 g

weight of $Mn(CH_3COO)_2 \cdot 4H_2O$ = 245.09 g/mol $\times$ (0.012315574 $\times$ 0.02 mol)

                                           = 0.0603 g

For example, 1 gram of $Zn_{0.98}Al_{0.01}Mn_{0.01}O$ can be prepared by following calculations;

mol of $Zn_{0.98}Al_{0.01}Mn_{0.01}O$ = 1 g/(85.845 g/mol)

                                           = 0.011648902 mol

weight of $Zn(CH_3COO)_2 \cdot 2H_2O$ = 219.50 g/mol $\times$ (0.011648902 $\times$ 0.98 mol)

                                           = 2.5057 g

weight of $Al(NO_3)_2 \cdot 9H_2O$ = 375.13 g/mol $\times$ (0.011648902 $\times$ 0.02 mol)

                                           = 0.0923 g

weight of $Mn(CH_3COO)_2 \cdot 4H_2O$ = 245.09 g/mol $\times$ (0.011648902 $\times$ 0.02 mol)
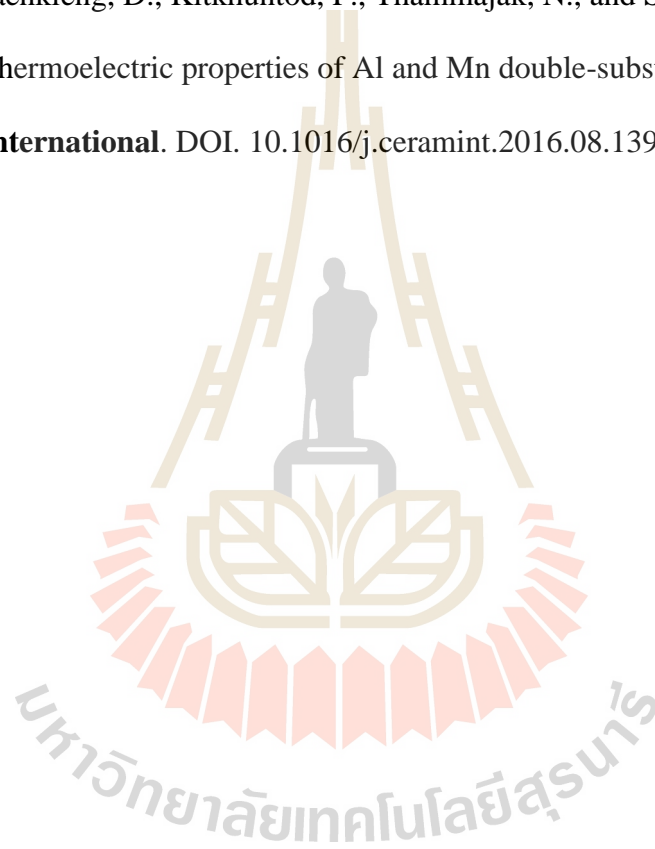
                                           = 0.0571 g

APPENDIX B

THESIS OUTPUT

Yong, N., Naenkieng, D., Kitkhuntod, P., Thammajak, N., and Siritanon, T. (in press). Thermoelectric properties of Al and Mn double-substituted ZnO. **Ceramic International**. DOI. 10.1016/j.ceramint.2016.08.139.

CURRICULUM VITAE

Name   Miss Nararat Yong

Date of Birth December 15th, 1990, Nakhonsrithammarat, Thailand

Address   4 Village no.3, Khungyan Sub-District, Thungyai District, Nakhonsrithammarat Province, Thailand, 80240

Education

2009-2012   B.Sc. (Chemistry), Thaksin University, Thailand

2013-2016   Student at department of chemistry, Suranaree University of Technology, Thailand

Publications

Yong, N., Naenkieng, D., Kitkhuntod, P., Thammajak, N., and Siritanon, T. (2016). Thermoelectric properties of Al and Mn double-substituted ZnO. **Ceram. Int.** DOI 10.1016/j.ceramint.2016.08.139.

Siritanon, T., Jiaprasertboon, A., and **Yong, N**. (2015). Structure and optical properties of $Ni_{1-x}Co_xWO_4$ solid solutions. **Mater. Lett.** 145: 316-320.